

A novel technique for nonlinear sensitivity analysis: Application to moist predictability

O. Rivière,^{a,b,c} G. Lapeyre^{a*} and O. Talagrand^a

^aLaboratoire de Météorologie Dynamique/IPSL, Ecole Normale Supérieure/CNRS, Paris, France

^bEcole Nationale des Ponts et Chaussées, Marne La Vallée, France

^cCentre National de Recherches Météorologiques, Météo-France, Toulouse, France

ABSTRACT: A new nonlinear technique is described to compute the sensitivity of synoptic perturbation growth to environmental moisture. The perturbation growth is defined using a nonlinear generalization of singular vectors called Nonlinear Singular Vectors (NLSV). For a given atmospheric state evolving in time, the nonlinear sensitivity method consists in maximizing the growth rate of perturbations by seeking both the optimal NLSV perturbations and the most favorable spatial distribution of the moisture field. This results in a new atmospheric state that differs initially only by the water vapour field. The NLSV computed along this new state has the largest possible growth rate for all possible water vapour fields. We apply this method to a simulation of the moist primitive equations. For the particular case we study, we obtain a moistening of the lower troposphere and an amplification of energy of optimal perturbations three times larger than the amplification of optimal perturbations computed without altering the water vapour field. The optimal perturbations are similar to the perturbations of the unmodified water vapour case. A noteworthy property is that the complete saturation of the atmosphere leads to a smaller increase in amplification rate, which means that the water vapour field is strongly tied to the NLSV structure. Mechanisms explaining these results are discussed. This technique overcomes the limitations (in particular the linearity assumption) of moist singular vector analysis using moist norms or adjoint sensitivity analysis. It can be applied to diagnose sensitivity to other fields as well. Copyright © 2009 Royal Meteorological Society

KEY WORDS baroclinic systems; singular vectors; perturbation growth

Received 22 July 2008; Revised 12 May 2009; Accepted 15 May 2009

1. Introduction

Mid-latitude atmospheric perturbations primarily develop through baroclinic instability. Although considerable attention has been paid to the dry dynamics of baroclinic instability, moist processes have long been thought to play a secondary role. However, recent studies suggest that diabatic effects may have played a predominant role in violent cyclogenetic events such as the December 1999 European storms *Lothar* and *Martin* (Wernli *et al.*, 2002; Hoskins and Coutinho, 2005). In the case of the storm *Lothar* (T1), a filament with high water vapour content (of width 300 km and length 2000 km) was observed in the region of development of the storm; an analysis by singular vectors (SVs, initial perturbations having a maximum growth rate over a given time period under the assumption of linear evolution) including moist physics, demonstrated that this filament was crucial for the storm intensification (Hoskins and Coutinho, 2005). Examining the sensitivity of singular vectors to the moist physics, Coutinho *et al.* (2004) showed that in most of the cases moist SVs resemble dry SVs but, on some occasions, new structures could occur. In addition

new mechanisms involving diabatic processes (such as the diabatic Rossby waves; Parker and Thorpe, 1995) as alternatives to the classical baroclinic mechanisms have been proposed to explain rapid development of synoptic systems. It was recognized both by theoretical studies (Lapeyre and Held, 2004) and by studies of individual cases (Hoskins and Coutinho, 2005) that the spatial distribution of water vapour compared to the distribution of potential vorticity is essential to promote the intensification of storms. If water vapour is present in the first phase of growth, it can efficiently intensify the storm. This means that the horizontal transport of water vapour plays a major role and needs to be further investigated, not at the scale of the storm, but at the scale of the storm track which creates a favourable background for subsequent storm development. Moist processes have been given some attention in predictability during the last decade (Beare *et al.*, 2003; Hohenegger and Schär, 2007; Spyksma and Bartello, 2007). Moreover, latent heat release may strongly modify nonlinearities of synoptic systems. Actually, synoptic eddies have very different properties for different water content in the atmosphere (Pavan *et al.*, 1999; Lapeyre and Held, 2004; Tan *et al.*, 2004; Moore and Montgomery, 2005). Increasing the atmospheric moisture content can have a dramatic effect on nonlinearities of the synoptic eddies, as one observes

*Correspondence to: Guillaume Lapeyre, Laboratoire de Météorologie Dynamique/IPSL, Ecole Normale Supérieure, 24 Rue Lhomond, 75005 Paris, France. E-mail: glapeyre@lmd.ens.fr

an abrupt transition from weakly nonlinear eddies for low water vapour content to intense coherent structures for higher water vapour content in quasi-geostrophic (QG) baroclinic simulations (Lapeyre and Held, 2004).

To better understand the role of water vapour in predictability, it is needed to quantify the sensitivity of synoptic systems to water vapour. For this purpose, we can rely on different methods that allow numerical measurement of the sensitivity to a particular physical process. A first method consists of performing integrations of the model, modifying with each integration specific parameters, or switching on or off specific parametrizations, in order to quantify the effects of those parameters or parametrizations on the dynamics. This has been done for instance by Moore and Montgomery (2004). This determines whether a particular process (such as latent heat release) is crucial or not in the intensification of extratropical cyclones. Following such an approach, Hoskins and Coutinho (2005) have compared dry and moist singular vectors. A drawback of comparing different simulations with some parametrization switched off or on is that this cannot precisely quantify the part played by the physical process in the dynamics. A more systematic method consists of computing the adjoint sensitivity of a particular function (e.g. surface pressure of a cyclone). Indeed, the adjoint model allows the computation of the gradient of any function of the forecast fields with respect to all the input parameters of the model and therefore provides a useful first-order approximation of the sensitivity (Talagrand, 1991; Rabier *et al.*, 1992, 1996; Errico, 1997). Using this technique, Langland *et al.* (1996) studied in an idealized case the effect of latent heat release on the development of a cyclone. They found that the sensitivity to moisture is very similar to the sensitivity to temperature, with a signal primarily in the region of strong precipitation. Moisture was shown to reinforce the dry baroclinic mechanism of growth. However the adjoint approach (and the SV analysis) relies on the linear assumption which may not be valid for strongly developing synoptic systems.

One method to take nonlinearity into account in the growth of perturbations has been proposed by Barkmeijer (1996). It consists of iteratively determining the (linear) SVs of model orbits emanating from a sequence of perturbations meant to approximate the fastest-growing perturbation. We take here a different approach, which derives in part from the method of Nonlinear Singular Vectors (NLSVs) introduced by Mu (2000). The NLSVs are the perturbations of given initial amplitude which grow most rapidly over a given period of time, in the full nonlinear dynamics. Rivière *et al.* (2008) have determined the NLSVs of the Phillips quasi-geostrophic model of baroclinic instability. Those NLSVs turn out to be very similar to linear SVs except that their spatial structure is modified to adapt to wave–wave and wave–mean flow interactions. They possess an initial shear (absent for the SV) that increases the total shear of the jet, in order to counteract the natural tendency of nonlinear baroclinic flows that decreases the shear. Also the spatial structure of NLSVs is more elongated than that

of SVs, which limits wave–wave interactions. Beare *et al.* (2003) have proposed an alternative approach based on a PV sensitivity map by computing numerous nonlinear integrations changing each time the location of a PV perturbation with a typical shape. However this method cannot take into account the complex geometry of the optimal perturbation since its shape is given *a priori*.

In the present paper, we combine the NLSV method and the sensitivity approach. Our technique is quite general but we choose to apply it here to the problem of the predictability of moist synoptic systems. It is described in section 2 together with its numerical implementation. We examine in section 3 the impact of moisture on the growth rate of baroclinic perturbations (for a given reference state). In section 4, we examine the results of our nonlinear sensitivity method on this reference state and propose some interpretation of it. In this paper, we choose to examine only one case of predictability because the focus of the paper is the description of the nonlinear technique. However we think that the moist processes we reveal might help to understand the interplay between baroclinic cyclogenesis and moisture. Conclusions are drawn in section 5.

2. Description of the nonlinear sensitivity for moist predictability

A classical way to quantify predictability is to compute SVs (Lacarra and Talagrand, 1988; Farrell, 1989; Buizza, 1994) which are perturbations of a given atmospheric state that amplify the most rapidly in the tangent linear regime. Based on this ingredient and adjoint sensitivity (which both use the adjoint of the model), it is possible to develop a new method to quantify the sensitivity of growth of optimal perturbations to a particular field.

Consider a reference model trajectory noted with initial condition $\mathbf{X}(t=0) = \mathbf{X}_0$ with \mathbf{X} the state vector in phase space. The time evolution of this trajectory will be noted $\mathbf{X}(t) = \mathbf{M}(\mathbf{X}_0)$. (We omit the time dependence in \mathbf{M} for simplification.) The nonlinear evolution of an initial perturbation $\delta\mathbf{x}(t=0) = \delta\mathbf{x}_0$ is $\delta\mathbf{x}(t) = \mathbf{M}(\mathbf{X}_0 + \delta\mathbf{x}_0) - \mathbf{M}(\mathbf{X}_0)$ (Figure 1(a)). The amplification of such a perturbation over a period τ is given by

$$\sigma^2(\delta\mathbf{x}_0) = \frac{E(\delta\mathbf{x}(\tau))}{E(\delta\mathbf{x}_0)}, \quad (1)$$

with $E(\delta\mathbf{x})$ the energy of the perturbation (to be defined below). The classical SVs are the perturbations that maximize the amplification function σ^2 when \mathbf{M} is the tangent linear model. Based on this idea, Mu (2000) proposed to introduce the nonlinear singular vector (NSV in his terminology) that maximizes $\sigma^2(\delta\mathbf{x}_0)$ over all possible $\delta\mathbf{x}_0$. However, this method does not take into account the fact that nonlinearities tend to decrease the growth rate, with the consequence that the largest growth rates will be obtained for infinitesimally small perturbations (which will be then identical with the SVs built on the tangent linear system). Mu *et al.* (2003)

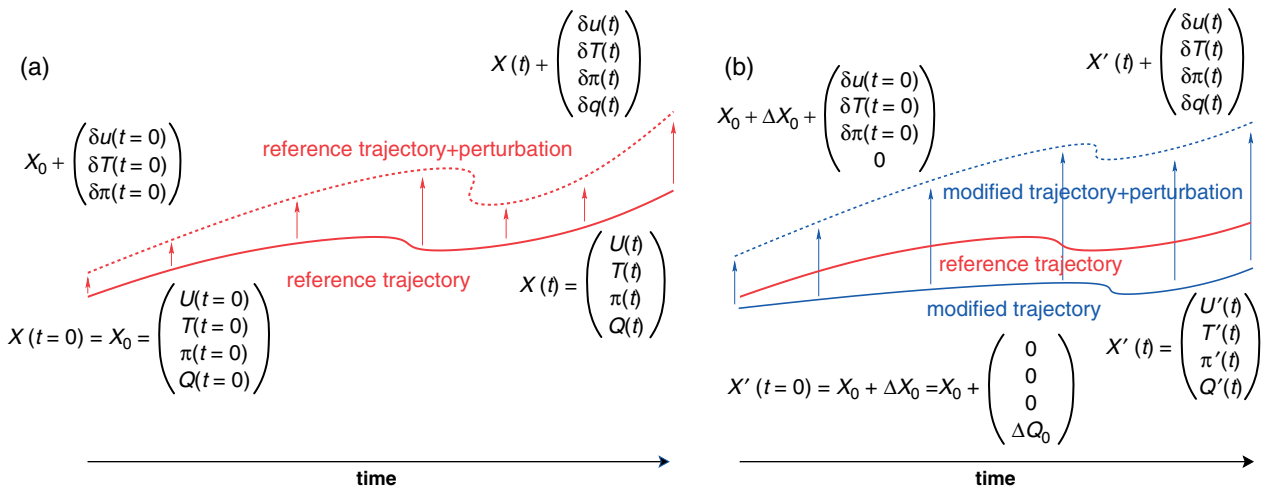


Figure 1. (a) Nonlinear optimal perturbation technique. The initial basic state X_0 defines a reference trajectory when evolving nonlinearly in the model and perturbations $\delta \mathbf{x}$ (vertical arrows) are computed as the difference between the nonlinear runs represented by the two curves. (b) Nonlinear sensitivity of optimal perturbations to environmental moisture. ΔX_0 modifies the basic state (to the lower continuous curve) and the perturbation $\delta \mathbf{x}$ is computed as in (a) from the modified trajectory. This figure is available in colour online at www.interscience.wiley.com/journal/qj

proposed to determine the perturbations that maximise the amplitude $E(\delta \mathbf{x}(\tau))$ under the constraint $E(\delta \mathbf{x}(0)) \leq E_0$. (Mu *et al.* (2003) noted that other possibilities for the constraint could exist.) Those perturbations are called Conditional Nonlinear Optimal Perturbations (CNOPs). After the CNOP method was proposed, Duan *et al.* (2004) first applied it in searching for the optimal precursor for ENSO events using a simple ENSO model, then Duan and Mu (2006) extended the CNOP method to investigate the decadal change of ENSO amplitude. Also, Mu and Zhang (2006) extended the CNOP method to an equivalent barotropic quasi-geostrophic model. Rivière *et al.* (2008) introduced NLSV, i.e. perturbations that maximize $\sigma^2(\delta \mathbf{x}_0)$ under the constraint $E(\delta \mathbf{x}(0)) = E_0$. One question is then whether the maximum of $E(\delta \mathbf{x}(0))$ can be reached in the interior of the sphere $E(\delta \mathbf{x}(0)) < E_0$, so that the CNOPs will be different from the NLSVs. The CNOPs and the NLSVs can be shown to be identical if the mapping $\mathbf{X}(0) \rightarrow \mathbf{M}(\mathbf{X}(0))$ is continuous and one-to-one. In the present case, two different initial states $\mathbf{X}(0)$ can lead, through condensation, to the same final state. The mapping is not necessarily one-to-one, and the CNOPs and NLSVs may be different for our problem.

Now, we modify the trajectory itself such that $X_0 + \Delta X_0$ is the reference trajectory along which we compute the NLSV. For such a trajectory, the equation for the perturbation reads

$$\delta \mathbf{x}(t) = \mathbf{M}(X_0 + \Delta X_0 + \delta \mathbf{x}_0) - \mathbf{M}(X_0 + \Delta X_0) \quad (2)$$

(Figure 1(b)). For the given reference state X_0 , the amplification of this perturbation depends on two quantities, namely ΔX_0 and $\delta \mathbf{x}_0$,

$$J(\Delta X_0, \delta \mathbf{x}_0) = \frac{E(\delta \mathbf{x}(t = \tau))}{E(\delta \mathbf{x}_0)} \quad (3)$$

since $\delta \mathbf{x}(t)$ depends on ΔX_0 through (2). Our choice for $E()$ is to use the total dry energy, defined

by

$$E(\delta \mathbf{x}) = \frac{1}{2g} \iiint_0^{p_0} \left\{ (\delta \mathbf{u})^2 + R T_{\text{ref}} (\delta \pi)^2 + \frac{c_p (\delta T)^2}{T_{\text{ref}}} \right\} dx dy dp, \quad (4)$$

where $\delta \mathbf{u} = (\delta u, \delta v)$, δT and $\delta \pi$ are respectively the perturbations of horizontal wind, temperature and logarithm of the surface pressure fields. T_{ref} is a reference temperature equal to 270 K and $p_0 = 1000$ hPa. Through the choice of the dry energy norm, moisture fields in the perturbations are set to zero at initial and final times. The use of moist norms for large-scale extratropical SV computations did not prove to lead to results that are significantly different from the dry ones even with moist physics (Mahfouf and Buizza, 1996; Ehrendorfer *et al.*, 1999). Because of the choice of a dry norm, the perturbations $\delta \mathbf{x}$ that will develop are initially dry but will carry moisture through their time evolution. They can be considered as a nonlinear counterpart of moist SV. The reason of relaxing the linear assumption is that it is not valid for moist processes since precipitation can be triggered as soon as water vapour reaches saturation.

The modification of the basic state flow will be only on the water vapour field, i.e. $\Delta X_0 = \Delta Q_0$ where Q is the moisture variable. We can thus measure the sensitivity of the perturbation growth to the moisture of the basic state. As we will see, this method is different from moist SV using moist norms (i.e. including water vapour in the norm (4)). The moisture perturbation of SV with moist norm does not add useful information as it is strongly linked to the temperature field. This is due to the linearization of the precipitation scheme (Ehrendorfer *et al.*, 1999): when water vapour condenses on the reference trajectory, the perturbation of water vapour is automatically forced to be proportional to the perturbation of its saturated value (i.e. $\delta Q = \delta Q_{\text{sat}}$).

Since Q_{sat} depends on temperature and pressure only (by the Clausius–Clapeyron relationship), the perturbation in saturated water vapour is proportional to the temperature perturbation, such that $\delta Q_{\text{sat}} = (\partial Q_{\text{sat}}/\partial T) \delta T$ (for a model with pressure, or sigma, as vertical coordinate). This means that, when condensation occurs on the reference trajectory, water vapour perturbation is no longer an independent variable but is proportional to the temperature perturbation. This is the main disadvantage of using moist norms in singular vectors. By modifying the reference trajectory itself (through ΔQ_0), we are able to circumvent this limitation.

The problem we want to solve is to find the optimal perturbation $\delta \mathbf{x}_0^*$ and the optimal moisture field ΔQ_0^* that satisfy

$$J(\Delta Q_0^*, \delta \mathbf{x}_0^*) = \max_{\Delta Q_0, \delta \mathbf{x}_0} J(\Delta Q_0, \delta \mathbf{x}_0) \tag{5}$$

under the constraints

$$E(\delta \mathbf{x}_0) = E_0 \quad \text{and} \quad 0 \leq Q_0 + \Delta Q_0 \leq Q_{\text{sat}}(T_0),$$

where $Q_0 + \Delta Q_0$ is the initial water vapour field of the modified trajectory and $Q_{\text{sat}}(T_0)$ is the saturated water vapour. If initially $Q_0 + \Delta Q_0$ were larger than saturation, the excess of water vapour would precipitate immediately and there would be an arbitrarily large source of potential energy by diabatic heating; this explains the last constraint in (5). Also we add a constraint on $\delta \mathbf{x}_0$, because the growth rate of perturbations will depend on their initial energy E_0 when evolving in the nonlinear model. For small initial energy, the perturbation will behave quasi-linearly (as an SV). For larger initial energy, the evolution can be quite different from the SV because of the development of nonlinearities, as shown by Rivière *et al.* (2008).

Equation (5) defines a standard problem in large-dimension constrained nonlinear optimization. It is not straightforward that an optimal solution of such a problem exists and is unique. However for a model with a finite number of degrees of freedom such as a general circulation model (GCM), one solution should exist at least. Only its physical meaning needs to be assessed. We solve problem (5) with a quasi-Newton BFGS (Broyden–Fletcher–Goldfarb–Shanno) algorithm called IPOPT (Interior Point Optimizer; Wächter and Biegler, 2006) already used in Rivière *et al.* (2008). The algorithm proceeds in minimizing the inverse of the cost function, i.e. $1/J(\Delta Q_0, \delta \mathbf{x}_0)$. It needs to evaluate the gradients of the function $J(\Delta Q_0, \delta \mathbf{x}_0)$ and of the constraint $E(\delta \mathbf{x}_0)$. These gradients are computed using the adjoint equations of the model. (The Appendix gives a detailed derivation.) The gradient of $J(\Delta Q_0, \delta \mathbf{x}_0)$ is given by

$$\frac{\partial J}{\partial (\delta \mathbf{x}_0)} = \frac{2}{E_0} \mathbf{M}_{|\mathbf{X}_0 + \Delta \mathbf{X}_0 + \delta \mathbf{x}_0}^* \mathbf{A} \delta \mathbf{x}(t = \tau) - \frac{2E_f}{E_0^2} \mathbf{A} \delta \mathbf{x}_0, \tag{6}$$

$$\frac{\partial J}{\partial (\Delta \mathbf{X}_0)} = \frac{2}{E_0} \mathbf{N}_{|\mathbf{X}_0 + \Delta \mathbf{X}_0 + \delta \mathbf{x}_0}^* \mathbf{A} \delta \mathbf{x}(t = \tau) - \frac{2}{E_0} \mathbf{N}_{|\mathbf{X}_0 + \Delta \mathbf{X}_0}^* \mathbf{A} \delta \mathbf{x}(t = \tau), \tag{7}$$

where $\mathbf{X}_0 + \Delta \mathbf{X}_0$ is the total reference state (taking into account ΔQ_0), $E_0 = E(\delta \mathbf{x}_0)$ and $E_f = E(\delta \mathbf{x}(t = \tau))$. \mathbf{A} is the matrix of the scalar product associated with the norm defined by (4). $\mathbf{M}_{|\mathbf{X}}^*$ is the projection on the dry variables of the adjoint model about the trajectory corresponding to the initial basic state \mathbf{X} . $\mathbf{N}_{|\mathbf{X}}^*$ is the projection on the moisture variable only. The algorithm also approximates the Hessian of J by the BFGS method. Further details can be found in Wächter and Biegler (2006). The algorithm stops when the optimality error

$$\epsilon_{\text{opt}} = \max \left\{ \left\| \nabla \left(\frac{1}{J(\Delta Q_0, \delta \mathbf{x}_0)} \right) + \mu \nabla c(\delta \mathbf{x}_0) \right\|_{\infty}, \alpha \left\| c(\delta \mathbf{x}_0) \right\|_{\infty} \right\}$$

becomes less than a specified error tolerance ϵ . The constraint c is defined by $c(\delta \mathbf{x}_0) = E(\delta \mathbf{x}_0) - E_0$. α is a scaling factor and μ the Lagrange multiplier for the constraints. The parameters α and μ are implicitly computed by the numerical algorithm and are of order unity. In practice, there is another constraint due to $0 \leq Q_0 + \Delta Q_0 \leq Q_{\text{sat}}(T_0)$ that is taken into account in ϵ_{opt} (Wächter and Biegler, 2006). We have found that the rate of convergence of the optimization depends on the spectral resolution and of the degree of nonlinearity of the problem. For the problem we solve here, around 150 iterations were needed to reach convergence. An important difference with linear SVs is that there is no guarantee to obtain a global maximum rather than a local one. Several minimizations have been performed here with different starting points in order to ensure that the final result does not depend on the initial condition. Furthermore with ΔQ_0 set to zero, we have checked that the optimal perturbation converges towards the leading SV as E_0 goes to zero (not shown).

Due to the inclusion of moist physics and precipitation in the nonlinear model, the gradient of the cost function is discontinuous and may not approximate the variation of the cost function when perturbing it around a given value. Indeed, large-scale precipitation and the associated latent heat release are triggered when moisture reaches the saturation threshold. The BFGS algorithm used for the optimization process is a gradient-based technique associated with a line-search method that gives the size of the step the algorithm will perform in the direction given by the Newton method (Wächter and Biegler, 2006) and theoretically requires the gradient of the cost function to be continuous. Similar difficulties have been encountered by the assimilation community when including physical processes of large-scale precipitation and convection in a 4D-Var assimilation algorithm. For instance, the study of Zou (1993) shows a slower convergence rate of the BFGS method when discontinuous processes were included without, however, hindering convergence towards the solution. This may be explained by the fact that the gradient of the cost function provides erroneous information to the optimization algorithm, because of the discontinuity. We performed 4D-Var experiments to see if we were able to retrieve water vapour through

a variational technique. From an initial known state considered as the real state of the atmosphere, we chose as the starting point for the 4D-Var a guess where the atmosphere was artificially saturated in a given target area. Using the energy of the difference of the true final state and the estimated one as a cost function, we found that the algorithm was able to reproduce the initial state, provided that the step size in the line-search procedure is not initially too small (Rivière, 2007).

3. Predictability analysis of a moist baroclinic situation

3.1. Short description of the numerical model

To obtain our basic state, we first run the PLANET SIMULATOR (PLASIM) developed by the University of Hamburg (Fraedrich *et al.*, 2005, provide a complete description) for 700 days at a spectral resolution of T63 with 15 vertical levels. The model is a GCM coupled with vegetation, ocean and sea-ice. Its atmospheric part is the PUMA2 model based on the primitive equations and is written in sigma coordinates. After the 700-day spin-up, we run for 2 days a modified version of PUMA2 that includes water vapour and simplified vertical diffusion, surface drag and large-scale precipitation. The two extra days of spin-up with the reduced physics package allow the

model to dissipate fast unbalanced motions due to the change in physics. Included parametrizations are present in a linearised form in the tangent linear and the adjoint model which has specifically been developed and validated (Rivière, 2007). No parametrization for convective precipitation is included in our physics package, since, according to Coutinho *et al.* (2004), it has a weak impact on the development of synoptic perturbations when compared to the impact of large-scale precipitation, at least for an optimization period of 24 hours.

We first compare the leading SV and NLSV in order to assess the influence of nonlinear processes in the growth of perturbations. NLSV has to our knowledge never been computed in a primitive-equation model.

We focus our attention on an extratropical baroclinic situation associated with the interaction of an upper-level structure and a surface system. Figure 2 shows the time evolution of the surface absolute vorticity and of the $\sigma = 0.73$ temperature. During this event, the anomalies seem to mutually amplify leading to the separation of an upper-level cyclone from the large-scale front over the United States. Associated with it, a tongue with a high moisture content is transported from the tropical regions and reaches the western coast of the United States (Figure 3). We will call this reference basic state the CONTROL experiment.

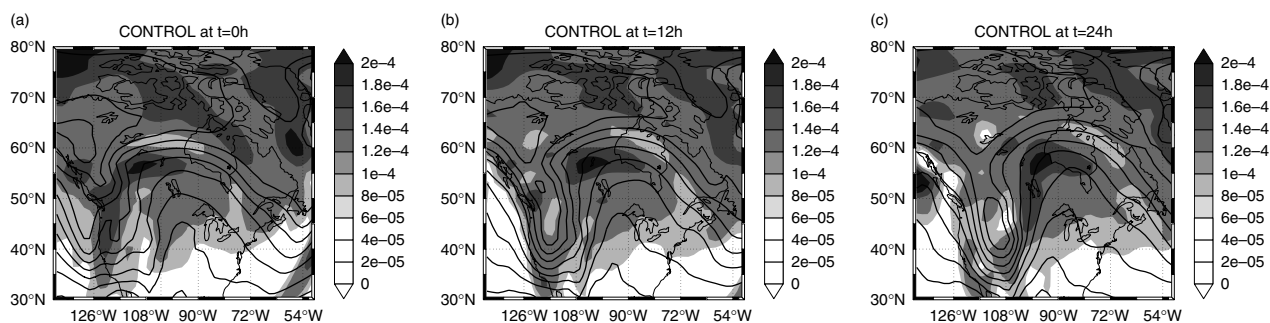


Figure 2. Surface absolute vorticity (s^{-1} ; grey shading) for the basic state of the CONTROL experiment at time (a) $t = 0$, (b) $t = 12$ hours and (c) $t = 24$ hours. Temperature contours at $\sigma = 0.73$ are superimposed.

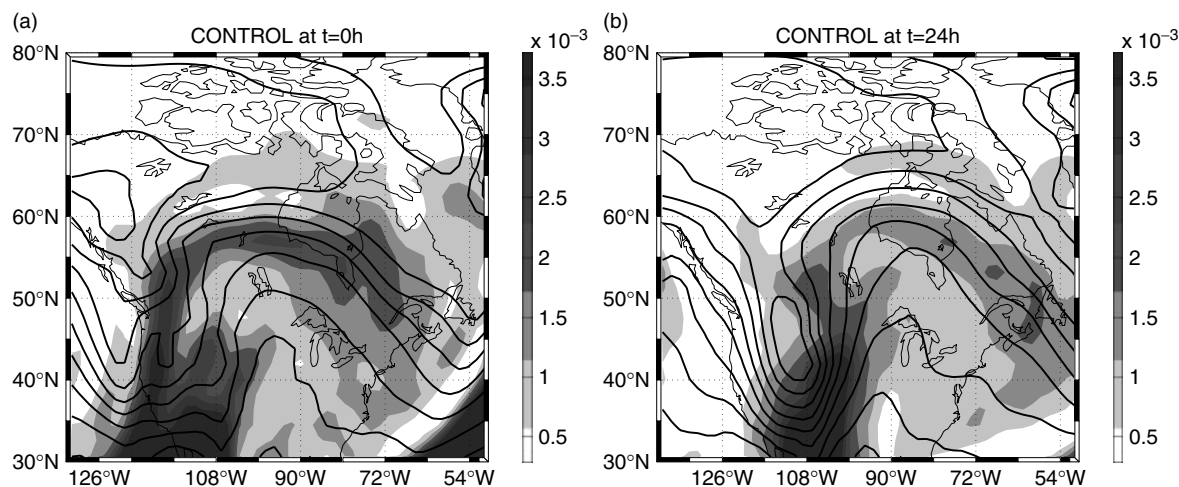


Figure 3. Specific humidity ($kg\ kg^{-1}$; grey shading) for the basic state of the CONTROL experiment at level $\sigma = 1$ at time (a) $t = 0$ and (b) $t = 24$ hours. Temperature contours at $\sigma = 0.73$ are superimposed.

3.2. Comparison of SV and NLSV for the CONTROL experiment

First of all, the NLSV ($\delta\mathbf{x}_0^\dagger$) is computed. It satisfies

$$J(\delta\mathbf{x}_0^\dagger) = \max_{\delta\mathbf{x}_0} J(\delta\mathbf{x}_0) \quad (8)$$

with $E(\delta\mathbf{x}_0) = E_0$.

Equation (8) is a particular case of (5) with ΔQ_0 set to zero. Optimal perturbations are computed over a 24-hour period for regions above 30°N . In the NLSV computation the initial energy E_0 is set such as to correspond to a maximal temperature amplitude of about 3 K at initial time and a maximum wind vector component of 4 m s^{-1} . NLSVs and SVs are computed with the model at full resolution (T63 and 15 vertical levels).

The detailed study of the properties of NLSV in a primitive-equation model is beyond the scope of this paper and will be the topic of a forthcoming paper. Here only main differences are presented but no interpretation is discussed. The NLSV exhibits features typical of SVs, such as a westward vertical tilt decreasing with time as shown in Figures 4(a, b, c). Also temperature perturbations propagate upward and downward. The NLSV perturbations are centred on the large-scale front in the baroclinic region and propagate eastward (Figures 4(d, e, f)). There is a spatial extension of the structure, as can be observed by comparing Figures 4(d, f). Although the NLSV evolves in the nonlinear model and the SV in the tangent linear model, both structures tend to be similar through the whole time integration (compare Figure 5 related to the dominant SV to Figure 4). However, small significant differences can be detected. For instance, the negative temperature NLSV perturbations tend to be located at higher altitudes and positive perturbations at lower altitudes than the SV (Figures 4(a) and 5(a)).

Energy amplification rates (σ^2) over 24 hours for the NLSV and for the leading SV evolving in the nonlinear and linear models are given in the first line of Table I. The NLSV $\delta\mathbf{x}_0^\dagger$ has an amplification rate of $\sigma^2 = 88.3$ in terms of total dry energy. In comparison, the leading SV has a linear growth rate of 98 which reduces to 70.4 when integrated through the nonlinear model. This shows that nonlinearities tend to limit the amplification, a known result in predictability (Snyder and Joly, 1998; Rivière *et al.*, 2008). The growth of the NLSV is larger than the growth of the leading SV in the nonlinear model, as expected from the definition of the NLSV. One advantage of nonlinear optimisation is that we obtain an optimal structure with a given sign (whereas SVs and $-$ SVs have the same growth rate when integrated in the tangent linear model). The influence of nonlinearities can be assessed by comparing the amplification of the NLSV and its opposite (i.e. when changing the signs of all the variables of the perturbation). SV and its opposite have a similar amplification (with a difference of growth of the order of 13%). This is in agreement with Gilmour *et al.* (2001) who showed that the evolution of SV over 24 hours is linear for amplitude of perturbation of the order of the

analysis uncertainty estimates. However the NLSV and its opposite display a difference of the order of 41% for the same initial energy as the linear SV. This means that the nonlinear optimal perturbation is able to take into account nonlinearities in its growth mechanism, as already observed by Rivière *et al.* (2008).

To evaluate the impact of moist processes on the growth, we computed the leading SV with latent heat release by large-scale precipitation being turned off. We observe a reduced amplification (dry SV in Table I), consistent with results of Coutinho *et al.* (2004). This could be expected since strong precipitation can be observed in the spatial region spanned by the SV (Figures 4(d, e)). We conclude that latent heat release plays a role in the perturbation growth although the basic mechanism for growth is baroclinic, as confirmed by the tilt against the shear in Figure 4(a). The atmospheric situation under study is thus typical of a baroclinic instability coupled with diabatic heating by moist processes.

3.3. Mechanisms for moist amplification of optimal perturbations

In agreement with previous studies on moist SVs (Coutinho *et al.*, 2004), the results from Table I show an increase of around 50% in the SV amplification when moist processes are turned on. To explain this increase, we can examine how moist processes trigger the amplification rate of perturbation. To this end, we use the linearized evolution equations for the perturbations. Indeed, the NLSV perturbations have dynamics close to the linear SV, in the sense that the spatial structure is very similar and only the amplification rate is reduced. In Rivière *et al.* (2008), the nonlinearities in the NLSV were shown to essentially affect wave-mean flow interactions. The NLSV differs from the SV by a large-scale component which increases the baroclinic instability of the flow. If we neglect this effect, the amplification due to moist processes reads through the potential energy equation,

$$\begin{aligned} \frac{1}{2} \frac{\partial(\delta T)^2}{\partial t} = & -\delta T(\mathbf{U}_0 \cdot \nabla \delta T + \delta \mathbf{u} \cdot \nabla T_0) \\ & -\delta T \left(\omega_0 \frac{\partial(\delta T)}{\partial p} + \delta \omega \frac{\partial T_0}{\partial p} \right) \\ & + \frac{\kappa}{p} (\omega_0 \delta T + \delta \omega T_0) \delta T + \delta \mathcal{J} \delta T, \end{aligned} \quad (9)$$

where δT , $\delta \mathbf{u}$, $\delta \omega$, $\delta \mathcal{J}$ are respectively the temperature, horizontal velocity, vertical velocity and diabatic heating of the NLSV and ∇ is the horizontal gradient (in pressure coordinates). The basic flow components are T_0 , \mathbf{U}_0 , ω_0 . The first two terms of (9) define the quantity C_a

$$C_a = -\delta T \left(\mathbf{U}_0 \cdot \nabla \delta T + \delta \mathbf{u} \cdot \nabla T_0 + \omega_0 \frac{\partial(\delta T)}{\partial p} + \delta \omega \frac{\partial T_0}{\partial p} \right), \quad (10)$$

which is the generation of potential energy by baroclinic processes. The third term C_e

$$C_e = \frac{\kappa}{p} (\omega_0 \delta T + \delta \omega T_0) \delta T \quad (11)$$

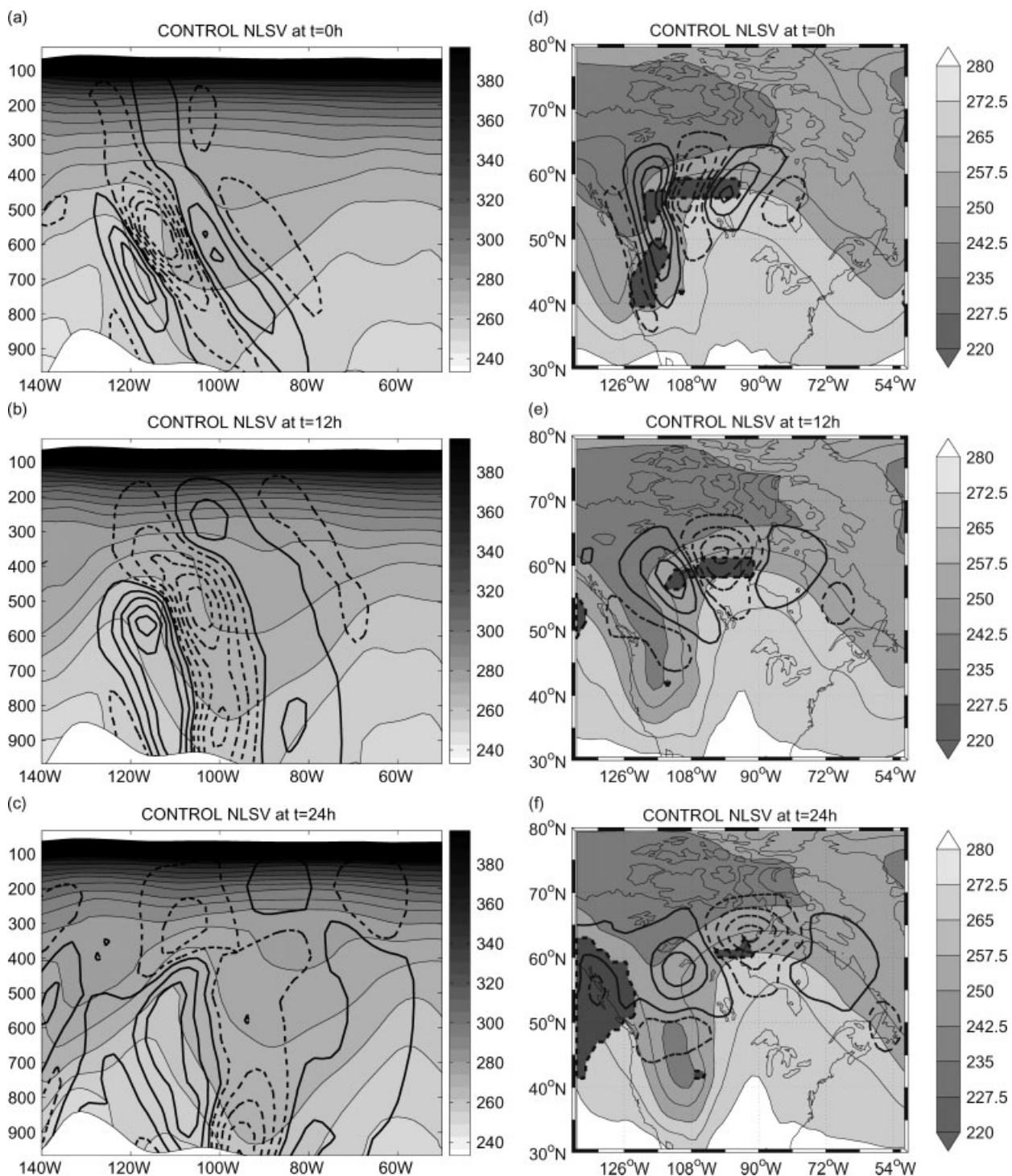


Figure 4. NLSV for the CONTROL experiment. (a–c) are vertical cross-sections at latitude 59°N showing temperature perturbations in bold contours at (a) $t = 0$ hours (with interval 0.5 K), (b) $t = 12$ hours (1 K interval) and (c) $t = 24$ hours (with contour interval 1.5 K). Solid contours are positive and dashed are negative. Grey shading is potential temperature (K). (d–f) are horizontal sections at $\sigma = 0.73$ at the same times, showing temperature perturbations in contours with interval as in (a–c), but additionally with temperature (K) as grey shading. On (d–f), dark shaded regions denote where vertical integrated precipitation occurs on the CONTROL basic state.

is the conversion of available potential energy (APE) into kinetic energy. The last term G_e

$$G_e = \delta \mathcal{J} \delta T \quad (12)$$

is the generation of APE by diabatic processes. It can be seen that moist processes amplify the perturbation growth

only if $\delta \mathcal{J} \delta T$ is positive, i.e. if the diabatic heating is in phase with the temperature perturbation. This is what is observed in our simulations (Figures 6(a–c)). Actually, the generation of APE through diabatic heating represents only 8% of the total generation of APE (Figure 7). It is maximum at 5 hours and decays to 4% at the end of the optimization time.

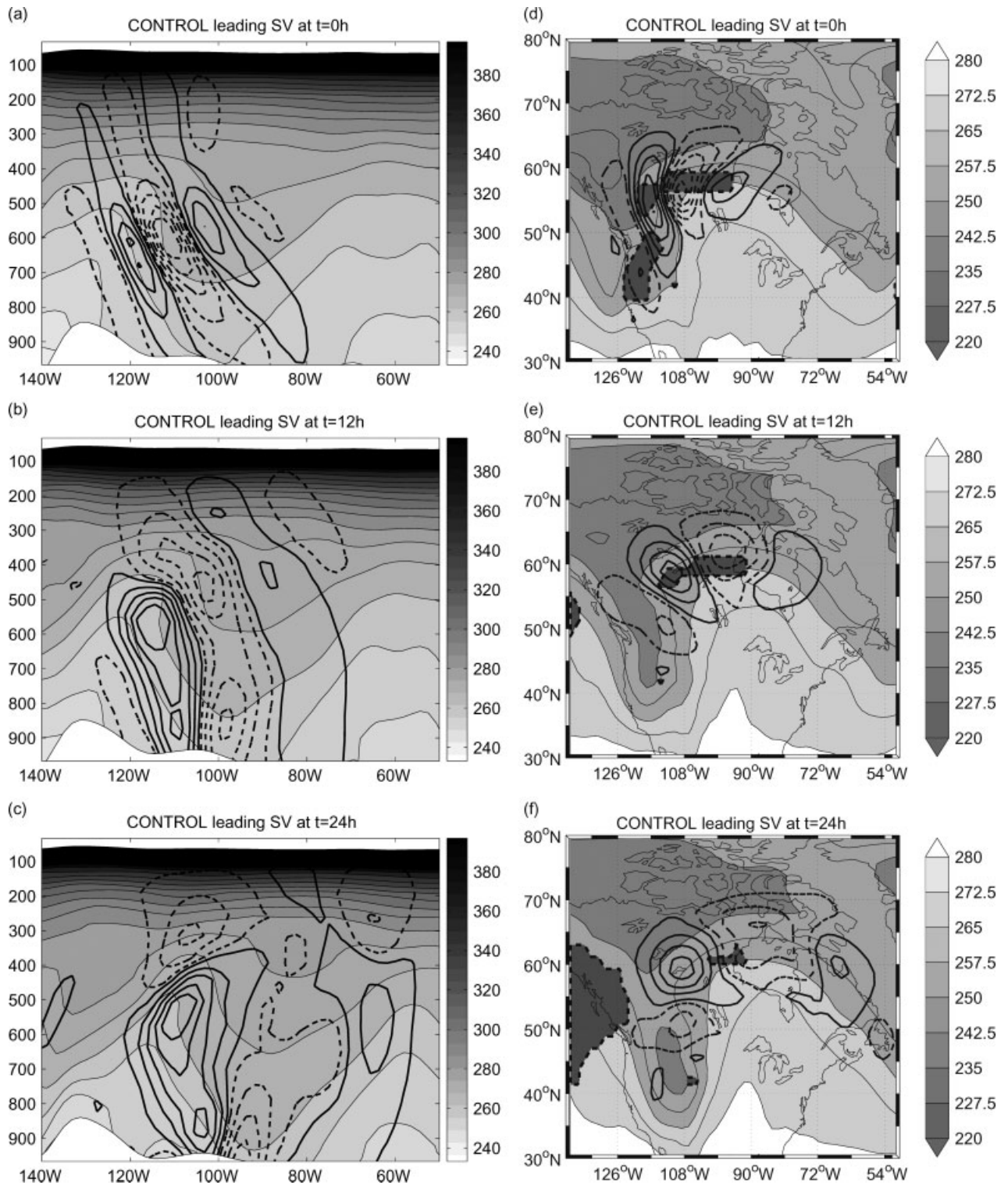


Figure 5. Leading SV for the CONTROL experiment. As Figure 4, but for the dominant SV (evolving in the tangent linear model).

Table I. Amplification rates, σ^2 , over 24 hours in terms of dry energy of the leading singular vector (SV1) and nonlinear optimal perturbation (NLSV) in the tangent linear (TL) and nonlinear (NL) models for the CONTROL and OPTIM experiments.

Initial perturbation	NLSV in NL	-NLSV in NL	SV1 in TL	SV1 in NL	-SV1 in NL	dry SV1 in TL
CONTROL	88.3	52.4	98.0	70.4	61.3	61.0
OPTIM	245.8	60.7	214.6	174.4	85.6	83.0

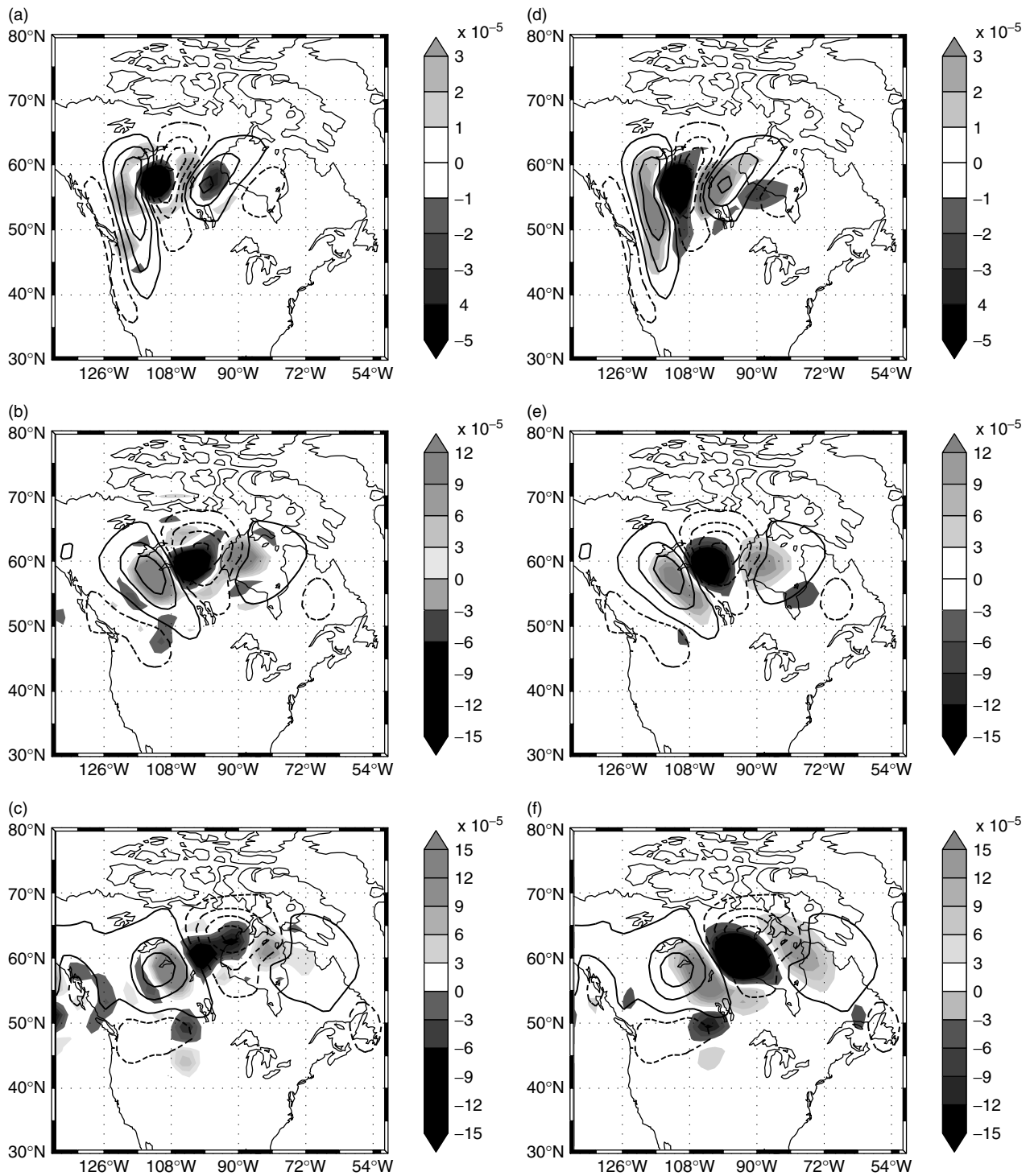


Figure 6. CONTROL experiment. δP ($\text{kg kg}^{-1} \text{h}^{-1}$; grey shading) for the NLSV at (a) $t = 0$ hours, (b) $t = 12$ hours and (c) $t = 24$ hours. (d–f) show the approximation of δP as computed from Equation (17) at the same times. NLSV temperature contours (bold solid lines for positive and dashed lines for negative) are superimposed. All quantities are evaluated at level $\sigma = 0.73$.

To explain the origin of the correlation of δJ and δT , we use arguments developed by Lapeyre and Held (2004). The linearized equation for the moisture perturbation δq reads

$$\frac{\partial(\delta q)}{\partial t} = -\delta \mathbf{u} \cdot \nabla Q_0 - \mathbf{U}_0 \cdot \nabla \delta q - \delta \omega \frac{\partial Q_0}{\partial p} - \omega_0 \frac{\partial \delta Q}{\partial p} - \delta P, \quad (13)$$

where Q_0 is the water vapour of the reference state and δP is the perturbation precipitation. To obtain the equation for δq_{sat} , we use

$$\delta q_{\text{sat}} = \left. \frac{\partial Q_{\text{sat}}}{\partial T} \right|_{T_0, p} \delta T \quad (14)$$

(since q_{sat} is a function of T and p only, and p is a coordinate) and the temperature equation to

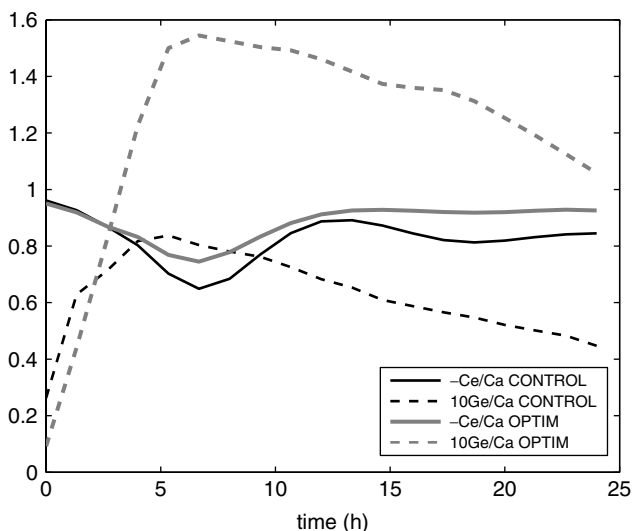


Figure 7. Conversion ratios C_e/C_a and G_e/C_a for the NLSV associated with the CONTROL and OPTIM experiments. Each term (C_e, C_a, G_e) is integrated over space.

obtain

$$\begin{aligned} \frac{\partial(\delta q_{\text{sat}})}{\partial t} = & -\mathbf{U}_0 \cdot \nabla \delta q_{\text{sat}} - \delta \mathbf{u} \cdot \nabla Q_{\text{sat}} \\ & - \omega_0 \frac{\partial(\delta q_{\text{sat}})}{\partial p} - \delta \omega \frac{\partial Q_{\text{sat}}}{\partial p} \\ & + \delta T \frac{\partial^2 Q_{\text{sat}}}{\partial T^2} \left(\frac{\kappa}{p} \omega_0 T_0 + \mathcal{J}_0 \right) \\ & + \frac{\partial Q_{\text{sat}}}{\partial T} \delta \mathcal{J} + \frac{\omega_0}{p} \frac{\partial Q_{\text{sat}}}{\partial T} \delta T (\kappa - 1) \\ & - \frac{\delta \omega}{p} \left(Q_{\text{sat}} - \kappa T_0 \frac{\partial Q_{\text{sat}}}{\partial T} \right), \end{aligned} \quad (15)$$

where Q_{sat} is the saturated water vapour of the basic state. The equation for the perturbed moisture deficit $\delta d = \delta q - \delta q_{\text{sat}}$ reads, using $\delta \mathcal{J} = L \delta \mathcal{P}/C_p$,

$$\begin{aligned} \frac{\partial(\delta d)}{\partial t} = & -\mathbf{U}_0 \cdot \nabla \delta d - \delta \mathbf{u} \cdot \nabla D_0 - \omega_0 \frac{\partial(\delta d)}{\partial p} - \delta \omega \frac{\partial D_0}{\partial p} \\ & - \delta T \frac{\partial^2 Q_{\text{sat}}}{\partial T^2} \left(\frac{\kappa}{p} \omega_0 T_0 + \mathcal{J}_0 \right) \\ & - \delta \mathcal{P} \left(1 + \frac{L}{C_p} \frac{\partial Q_{\text{sat}}}{\partial T} \right) - \frac{\omega_0}{p} \frac{\partial Q_{\text{sat}}}{\partial T} \delta T (\kappa - 1) \\ & + \frac{\delta \omega}{p} \left(Q_{\text{sat}} - \kappa \frac{\partial Q_{\text{sat}}}{\partial T} T_0 \right), \end{aligned} \quad (16)$$

where $D_0 = Q_0 - Q_{\text{sat}}$. In regions where precipitation occurs in the reference state ($\mathcal{P}_0 > 0$), moisture is at saturation (i.e. $Q_0 - Q_{0\text{sat}}$ is close to zero) and, because of the linearization of the precipitation operator, the perturbation δd is close to zero as well. The terms proportional to $\delta T \omega_0$ are in general small compared to the terms proportional to $\delta \omega T_0$ (not shown). Hence, the leading terms in (16) correspond respectively to the

effect of precipitation and of adiabatic expansion. The perturbation precipitation can be approximated by

$$\delta \mathcal{P} \approx \frac{Q_{\text{sat}} - \kappa T_0 \frac{\partial Q_{\text{sat}}}{\partial T}}{1 + \frac{L}{C_p} \frac{\partial Q_{\text{sat}}}{\partial T}} \frac{\delta \omega}{p}. \quad (17)$$

We can note that this kind of approximation is very similar to the parametrization for diabatic heating proposed by Emanuel *et al.* (1987). Figures 6(d–f) show the right-hand side of (17) at different times for the NLSV. This compares relatively well with perturbation precipitation in Figures 6(a–c), even if here we did not mask non-condensing regions. To see further if this approximation is valid in regions of precipitation, we computed the linear correlation coefficient between the two sides of (17), masking the regions with no precipitation. As can be seen in Figure 8(a), the correlation is close to 0.9 between 3 and 15 hours, decreasing to 0.7 at the end of the optimization period for the NLSV perturbations. (Correlations between 0 and 3 hours should not be trusted because initially there is some adjustment in the perturbation fields.) As the NLSV is subject to nonlinearities, we computed the same correlation coefficient for the SV in the tangent linear model (dashed curve on the same figure). Here the correlation stays close to 0.9, showing that in the linear approximation, (17) is valid.

Using $\delta \mathcal{J} = L \delta \mathcal{P}/C_p$ and (17), we obtain that the diabatic heating term in (9) depends on the correlation between the temperature δT and the vertical velocity $\delta \omega$. For baroclinically unstable flows, we expect a conversion from potential to kinetic energy which positively correlates these two quantities. This is indeed observed in our simulation, and was also documented by Gutowski *et al.* (1992) on longer time-scales, and by Zhang *et al.* (2007) for mesoscale flows. The idea underneath this result is that diabatic heating is associated with a decrease in the effective static stability of the flow (Emanuel *et al.*, 1987; Lapeyre and Held, 2004) which intensifies the baroclinic instability in condensating regions. This naturally increases the growth rate of the perturbation, but affects only weakly its spatial characteristics.

4. Nonlinear sensitivity to the environmental moisture

4.1. Description of the experiment

We now apply the complete technique described in section 2; the optimization is carried on both $\delta \mathbf{x}_0$ and ΔQ_0 , leading to a new trajectory and a new set of optimal perturbations (with respect to the new trajectory). The newly obtained trajectory $\mathbf{X}'(t) = \mathbf{M}(\mathbf{X}_0 + \Delta Q_0^*)$ will be called OPTIM. Table I reveals an unexpected result: the amplification of the optimal perturbation grows from $\sigma^2 = 88.3$ (for CONTROL) to 245.8 (for OPTIM), i.e. a strong increase, by almost a factor 3, of the amplification rate of the NLSV. A similar increase is observed for the moist leading SV for the OPTIM trajectory.

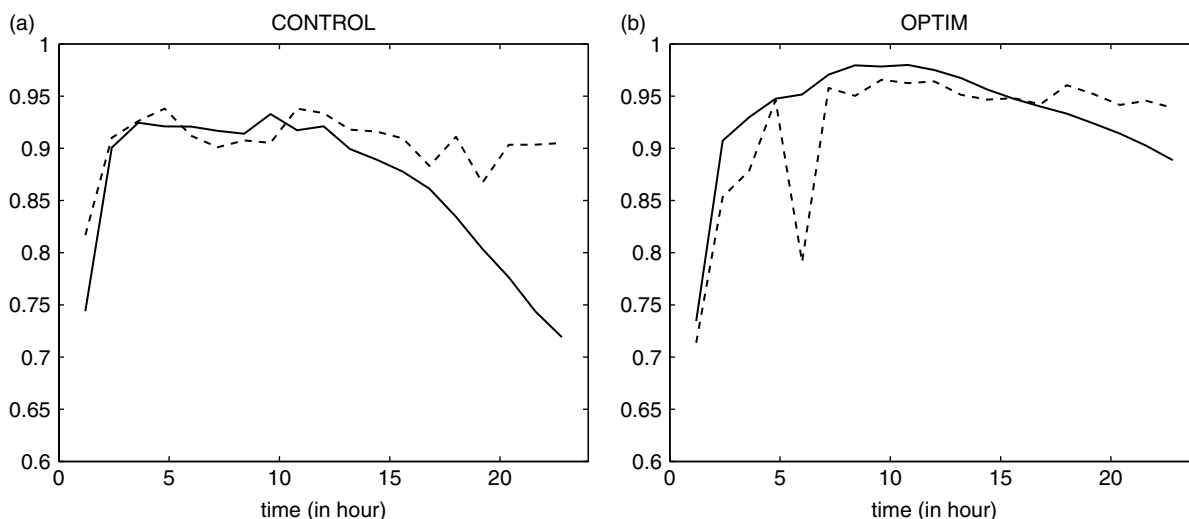


Figure 8. Correlation coefficient of r.h.s. of Equation (17) with perturbation precipitation as a function of time for experiments (a) CONTROL and (b) OPTIM. In each case, only regions with precipitation larger than a specific small threshold were taken into account. The continuous curve is for the NLSV, the dashed curve is for the SV.

In spite of those very different amplification rates in perturbation, the CONTROL and OPTIM integrations are similar (cf. vertical cross-sections of potential temperature on Figures 4(b,c) and 9(b,c) and horizontal cross-sections of temperature on Figures 4(e,f) and 9(e,f)). The modification of moisture in OPTIM has only a weak impact on the evolution of the system. The cyclone seems to form more rapidly in OPTIM (cf. Figures 4(f) and 9(f)). Also the basic state of OPTIM seems more statically unstable than the CONTROL trajectory (cf. Figures 9(b) and 4(b) at 110°W and 600 hPa). This is accompanied by stronger precipitation. The difference of the two velocity fields in terms of mean kinetic energy is at most $2\text{ m}^2\text{ s}^{-2}$. The maximum velocity difference is 20 m s^{-1} and the maximum temperature difference is 6.5 K, both near 400 hPa.

To see if the two trajectories are similar in terms of dry dynamics, we computed the amplification of dry SV for CONTROL and OPTIM. Here dry SVs are computed by setting the latent heat release to zero in the tangent linear model. The growth rate increases from $\sigma^2 = 61$ to 83 (Table I) which shows a modest change of the amplification. Also the dry SV structures resemble each other (not shown). We hypothesize that the larger amplification in OPTIM is due to a smaller static stability: the precipitation induced by ΔQ_0^* occurs at the lowest levels of the model and not in the middle troposphere as in the CONTROL experiment, which results in a destabilization of the atmosphere through heating. Indeed the spatially averaged static stability over the region decreases by 7% between the two experiments. If the growth rate is given by the Eady index $f_0 \partial_z u / \sigma$, then the amplification should become $61^{1.07} \approx 81$, which compares well with the observed value.

In the optimization process, we seek both the most favourable moisture environment and the fastest growing perturbations. These perturbations are *a priori* different from the perturbations of the CONTROL experiment.

Indeed the numerical algorithm that computes the OPTIM solution starts from a random initial condition. However, as can be seen in Figure 9 (cf. Figure 4), the spatial structure of the OPTIM NLSV $\delta \mathbf{x}_0^*$ is very similar to the CONTROL NLSV $\delta \mathbf{x}_0^\dagger$. The similarity index defined by Buizza (1994) is equal to 0.92 at the initial time. The similarity index of $\delta \mathbf{x}^\dagger$ and $\delta \mathbf{x}^*$ is computed here as the projection coefficient of $\delta \mathbf{x}^\dagger$ on the subspace spanned by $\delta \mathbf{x}^*$ using the dry energy norm, which allows us to compare the subspaces spanned by both NLSV. This coefficient ranges between zero (for orthogonal subspaces) and 1 (for identical subspaces). This means that the CONTROL and OPTIM NLSVs initially share 92% of energy in common. At the final time, the similarity index remains rather large, close to 0.88. For further comparison, we perturbed the CONTROL basic state with the OPTIM NLSV and vice versa. In the first case, the perturbation amplifies by a factor $\sigma^2 = 81.7$, and by a factor 208 in the second case. As there is only 10% difference between these amplifications rates and the original ones (88.3 and 245.8), this means that the perturbations are almost the same. This provides further evidence that it is the rearrangement of the moisture field that enhances the growth rate (through a larger release of potential energy by diabatic heating) and not the change in the basic structure of the perturbation.

Figure 10 shows the relative humidity at initial time for the CONTROL and OPTIM experiments. We observe that lower tropospheric layers tend to be saturated in more regions in OPTIM than in CONTROL. On the contrary, upper-tropospheric layers tend to be saturated in less regions. This results in a larger precipitation area in OPTIM than in CONTROL (cf. Figures 4(d–f) and 9(d–f)). Overall, the modification of the water vapour obtained in the OPTIM experiment seems reasonable. The optimization of both the environmental water vapour and the nonlinear perturbations does not lead to unphysical results, which gives some confidence on the relevance

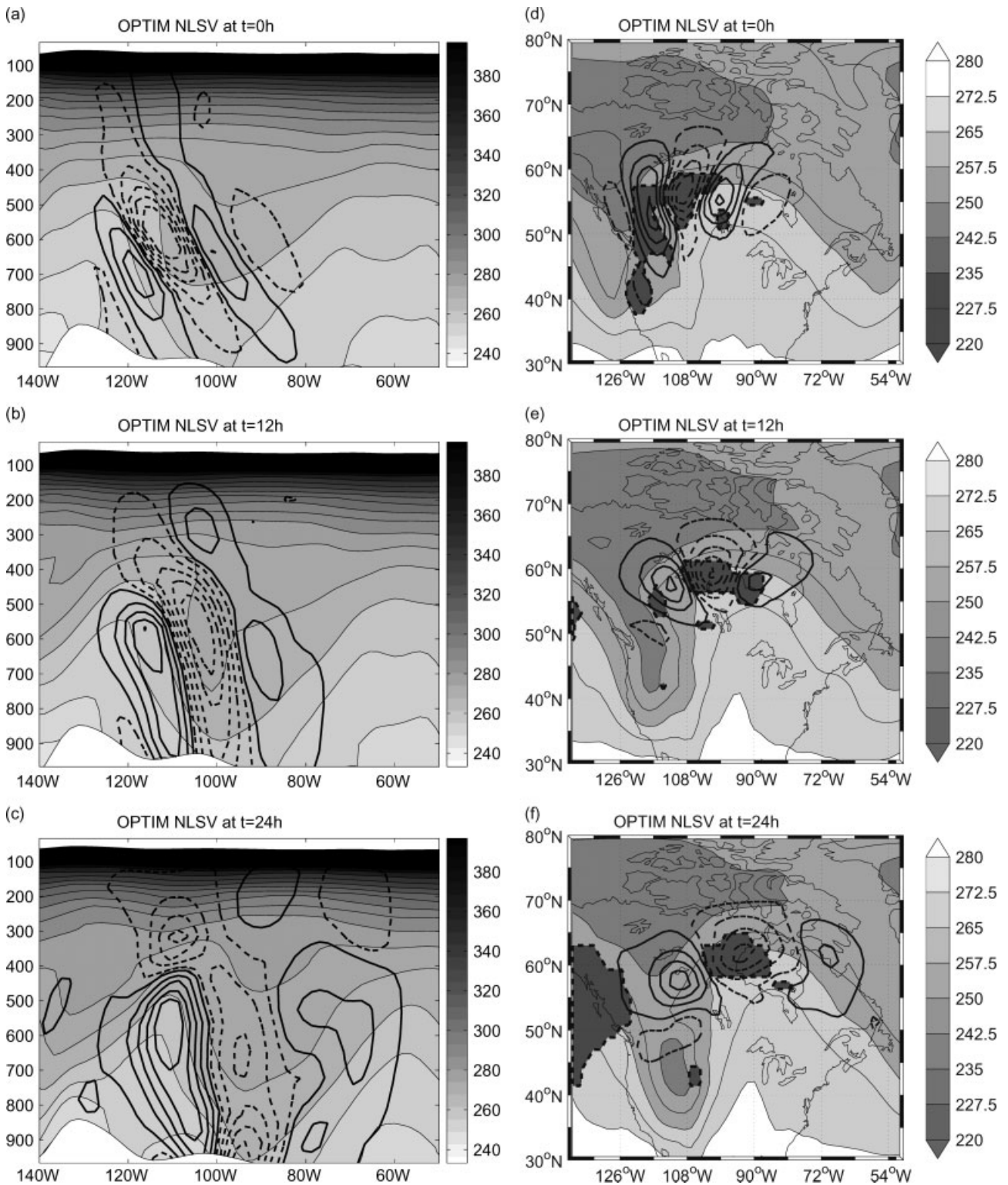


Figure 9. As Figure 4, but for the OPTIM experiment. NLSV are shown as bold temperature contours at intervals (a, d) 0.5 K, (b, e) 1.4 K, and (c, f) 2.8 K.

of the method. An important point is that we cannot claim uniqueness of the solution of the optimization problem (nor that we reached a global extremum). Nevertheless, the moisture modification ΔQ_0^* of the basic state dramatically increases the amplification of perturbations. In the following section we propose some physical mechanisms to explain our results.

4.2. The location of the optimal moisture

Figure 11 shows the optimized moisture environment ΔQ^* at different times. Initially ΔQ^* is positive in the lowest levels of the model mainly below 850 hPa. It is then advected horizontally and vertically by the basic flow. This perturbation remains to the south of the

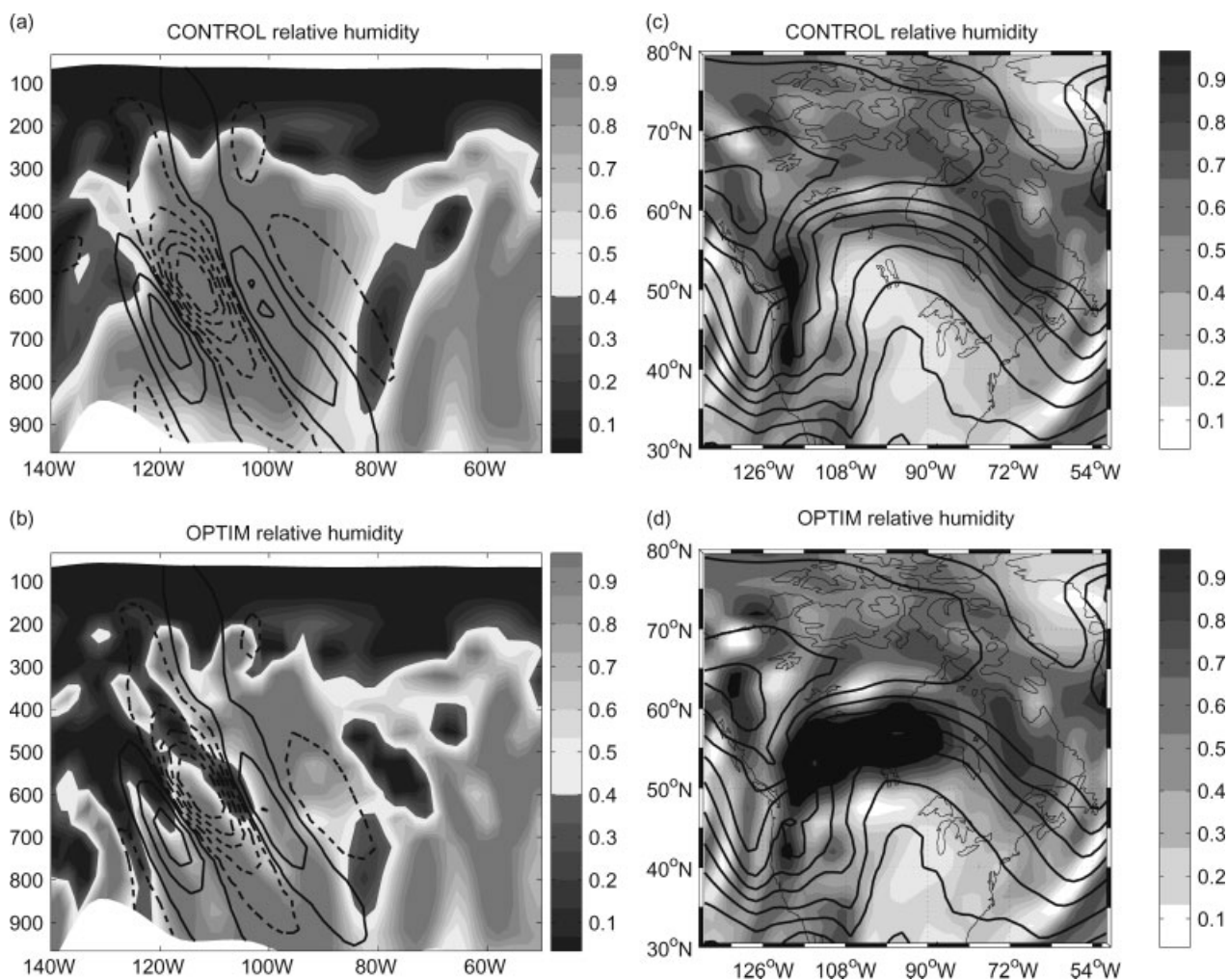


Figure 10. Relative humidity at $t = 0$ hours. (a, b) are vertical cross-sections at latitude 59°N , with contours of the NLSV temperature field superimposed, and (c, d) are horizontal sections of relative humidity at $\sigma = 1$, with contours of the basic state temperature (at $\sigma = 0.73$) superimposed. (a, c) are for the CONTROL experiment and (b, d) the OPTIM experiment.

NLSV structure. The OPTIM trajectory is saturated in less regions in the upper atmosphere, as is shown by relative humidity for CONTROL and OPTIM (Figure 10). As expected, it is closer to saturation near the surface than CONTROL.

The effect of the moisture distribution on perturbation growth was also examined by Pavan *et al.* (1999) and Tan *et al.* (2004). These authors showed that adding moisture on the southern part of a baroclinic front led to a larger perturbation growth, and we obtain here a similar result. It is worthwhile examining whether saturating the whole lower atmosphere would lead to the same conclusion. To that end, we did two experiments keeping the same dry initial basic state but saturating the whole region between 140°W and 60°W and between 40°N and 80°N and levels either under 700 hPa or above 700 hPa. In these experiments, we examined the evolution only of the NLSV δx_0^* of the OPTIM trajectory, since the NLSV structure does not seem to change much between CONTROL and OPTIM. Amplification of the NLSV was between $\sigma^2 = 120$ and 140 depending on the experiments. Such low increase in the amplification compared to the experiments using the optimal moisture

perturbation can be explained by the destruction of the baroclinicity. We indeed observed a decrease of the vertical shear of the wind induced by large latent heat release in the middle troposphere (not shown). Therefore, the distribution of water vapour that helps in the growth rate of the perturbation strongly depends on the characteristics of the flow field, in particular on the position of the large-scale front.

The generation of the APE of the perturbations through diabatic heating almost doubles between CONTROL and OPTIM, as can be seen in Figure 7. To understand why, we examine the efficiency of the mechanism described in section 3.3 by computing the correlation of the two terms of (17) for the NLSV in the OPTIM experiment. Figure 8(b) shows that the correlation is even higher than in the CONTROL experiment for both the SV and the NLSV. For the NLSV the correlation is still as large as 0.88 at the end of the optimization period. This result indicates that diabatic APE generation is more efficient in OPTIM. At the same time, the area of precipitation is twice as large in OPTIM as in CONTROL after 10 hours of integration (Figure 12). Both phenomena explain why the diabatic mechanism is very efficient in fostering the

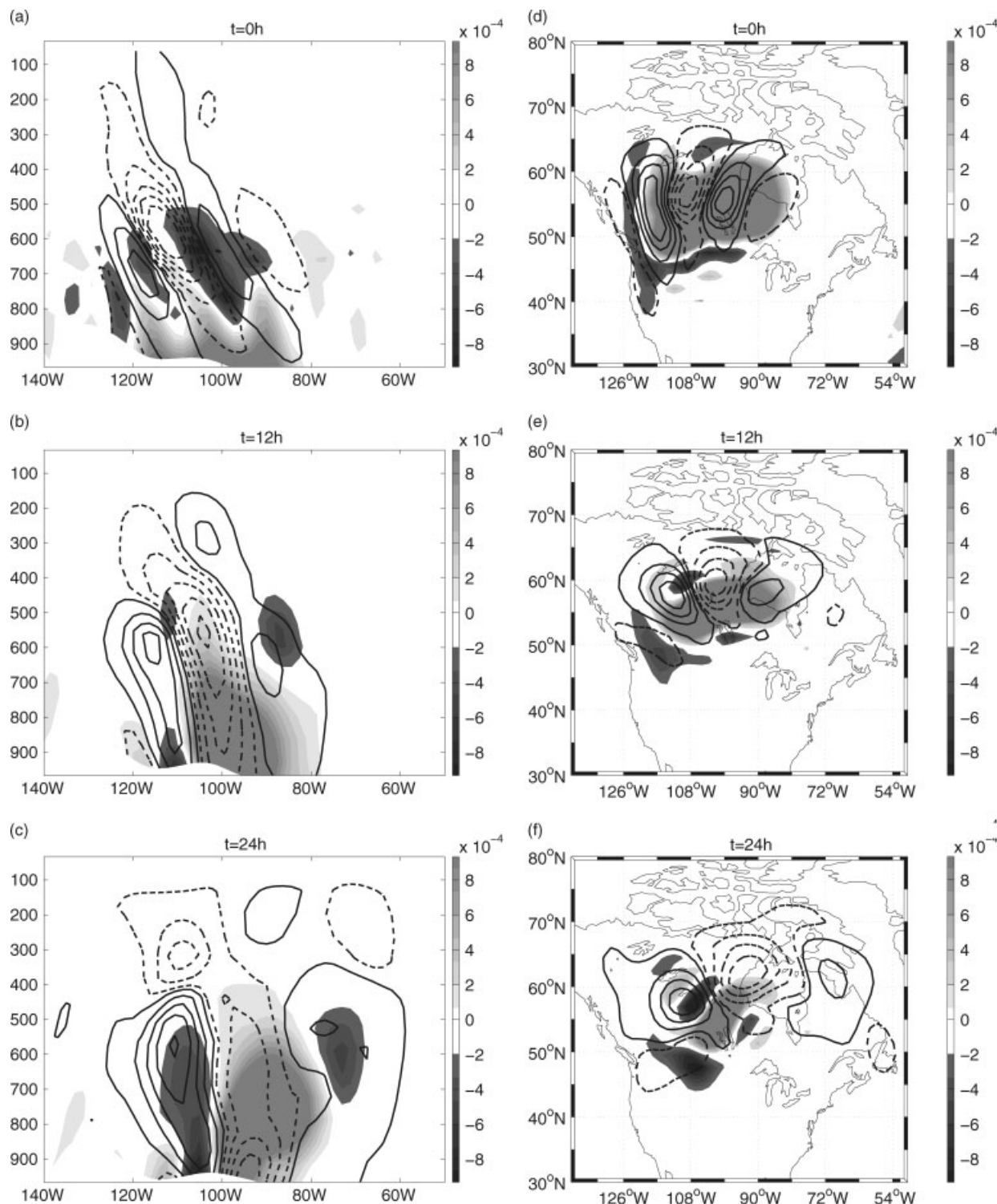


Figure 11. ΔQ^* (grey shading): vertical cross-sections at latitude 59°N at (a) $t = 0$ hours, (b) $t = 12$ hours, and (c) $t = 24$ hours. (d–f) are horizontal sections at $\sigma = 1$ at the same times. Superimposed are the NLSV temperature contours (bold) of the OPTIM basic state (at level $\sigma = 0.73$ in (d–f)).

growth of the perturbations. The comparison of perturbation energy growth in OPTIM and CONTROL shows that the APE rates of growth first separate after 5 hours, followed by the kinetic energy rate of growth after 10 hours (Figure 13). This is consistent with the precipitation area which shows that precipitation occurs more frequently in OPTIM than in CONTROL after 5 hours.

4.3. Impact of the nonlinearities in the OPTIM experiment

The consequence of the optimization of the water vapour field is that the perturbations are strongly sensitive to nonlinearities. Indeed, the opposite of NLSV ($-NLSV$) has its growth rate diminished by 75% compared to

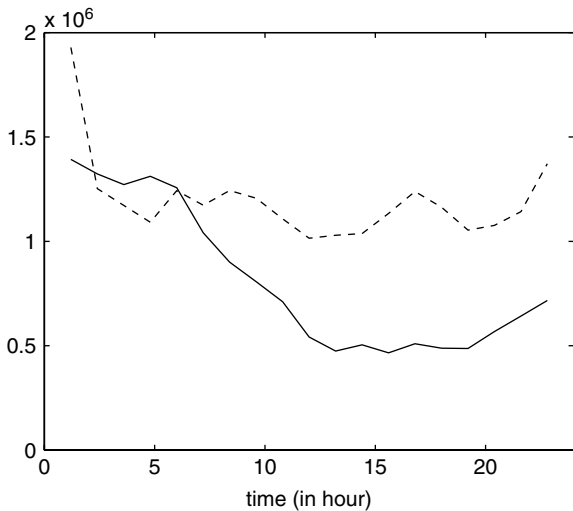


Figure 12. Precipitation area (km^2) inside the region $30\text{--}80^\circ\text{N}$, $130\text{--}54^\circ\text{W}$ for the CONTROL trajectory (solid curve) and OPTIM (dashed curve) as a function of time.

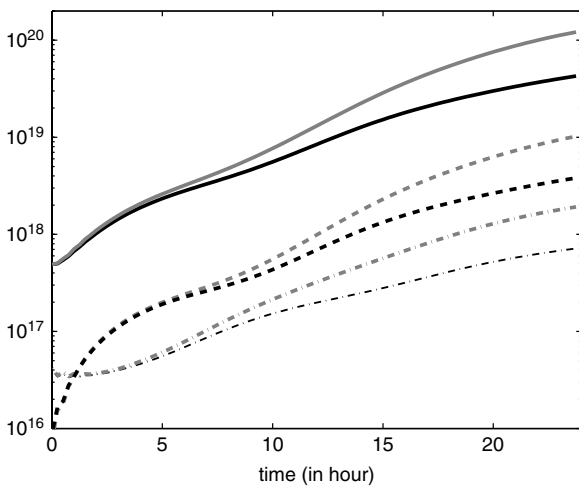


Figure 13. Energies for the CONTROL (black) and OPTIM (grey) experiments as a function of time: Total energy of the NLSV (solid), APE (dash-dotted), and kinetic energy (dashed). The total energy is shifted by a factor of 10 for clarity.

the NLSV, whereas the decrease was only 40% in the CONTROL experiment (Table I).

One possible explanation comes from the observation that the precipitation $P + \Delta P$ of the OPTIM basic state occurs mainly in regions where the temperature of the optimal perturbation $\delta\mathbf{x}^*$ is negative (cf. Figures 14(a) and (b)). This has to do with nonlinearities in the precipitation scheme. To explain that, we can consider the unperturbed reference state \mathbf{X} and the perturbed state vector $\mathbf{X} + \delta\mathbf{x}$ with the perturbation $\delta\mathbf{x}$ evolving in the nonlinear model. The precipitations on both trajectories ($P + \delta P$ and P) must be positive by definition. Two cases are possible. If δP is negative, it is bounded by the condition $|\delta P| < P$. If δP is positive, there is no such constraint and the dynamics are solely responsible for the value of δP . Now, if we modify P by adding ΔP (assuming the dynamics to remain unchanged) in regions with negative

δP , we have a new constraint $|\delta P| < P + \Delta P$. As explained in section 3.3, we know that the precipitation perturbation δP is positively correlated with the temperature perturbation δT . If we are able to modify the precipitation of the trajectory by ΔP (keeping the temperature perturbations the same), it is more efficient to increase the precipitation $P + \Delta P$ in regions where temperature perturbations are negative, so that δP can be larger, leading to an increase of diabatic heating. This is confirmed by Figure 14, which shows that for the OPTIM trajectory, $P + \Delta P$ reaches high values in regions where δT is negative. It allows δP to grow in the same time as δT , thereby generating potential energy by diabatic heating. This effect is purely nonlinear since in the tangent linear model perturbations are assumed to be infinitesimal. This explains why changing the sign of NLSV gives very different growth rates in the nonlinear model.

4.4. Differences between linear and nonlinear sensitivity

To see how our nonlinear sensitivity method compares with the standard technique of adjoint sensitivity, we computed the adjoint sensitivity to moisture for the CONTROL NLSV perturbation. Figure 15 shows that the linear sensitivity of J to moisture at initial time is larger in mid-atmosphere. The pattern of $\partial J / \partial Q_0$ is similar to what Langland *et al.* (1996) observed in their idealized extratropical cyclogenesis study. The signal in the middle troposphere is very similar to the ΔQ_0^* field (cf. Figure 11(a)). However a strong difference is that our method produces an increase of water vapour near the surface that is completely absent from the adjoint sensitivity field. This shows the usefulness of computing an optimal water vapour field using the fully nonlinear system since this increase in surface moisture is essential for the development of perturbations.

It is important to stress that the nonlinear sensitivity we discuss is different from classical adjoint sensitivity. Using an adjoint method, we cannot determine even the exact first-order sensitivity that we determine with our nonlinear method, and therefore we cannot expect the two methods to agree, even for small perturbations. The NLSV $\delta\mathbf{x}^*$ is indeed dependent on the modification of the water vapour of the basic state ΔQ_0 . Using the chain rule for the derivative of the optimal value of the cost function $J^*(\Delta Q_0, \delta\mathbf{x}^*)$, one can see that

$$\frac{\partial J^*}{\partial(\Delta Q_0)} = \frac{\partial J}{\partial(\Delta Q_0)} + \frac{\partial J}{\partial(\delta\mathbf{x})} \bigg|_{\delta\mathbf{x}^*, \Delta Q_0} \frac{\partial(\delta\mathbf{x}^*)}{\partial(\Delta Q_0)}. \quad (18)$$

Because of the constraint on the initial energy, we do not have $\partial J / \partial(\delta\mathbf{x}) = 0$ at the optimum. Actually $\partial J / \partial(\delta\mathbf{x})$ is a function of the Lagrange multiplier for the problem. This means that the gradient of the cost function *along* the optimum perturbation (left-hand side of (18)) is different from the gradient of the cost function at the optimum (first term on the right-hand side). Furthermore, the expression of $\partial(\delta\mathbf{x}^*) / \partial(\Delta Q_0)$ requires the knowledge of the second-order derivatives (Le Dimet *et al.*, 1997).

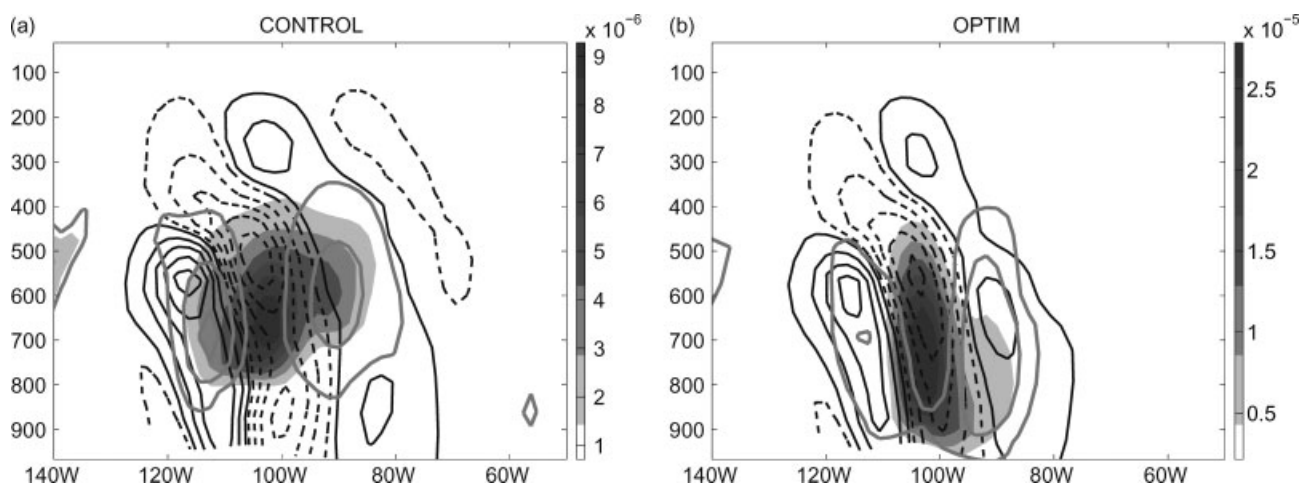


Figure 14. Vertical cross-sections at 59°N of the precipitation field (grey shading) at 12 hours for (a) the CONTROL trajectory (i.e. P), and (b) the OPTIM trajectory (i.e. $P + \Delta P$). Also shown are total precipitation (i.e. $P + \delta P$ and $P + \Delta P + \delta P$; grey solid contours), and temperature perturbation of the NLSV in thin contours (i.e. δT ; black solid for positive, dashed for negative).

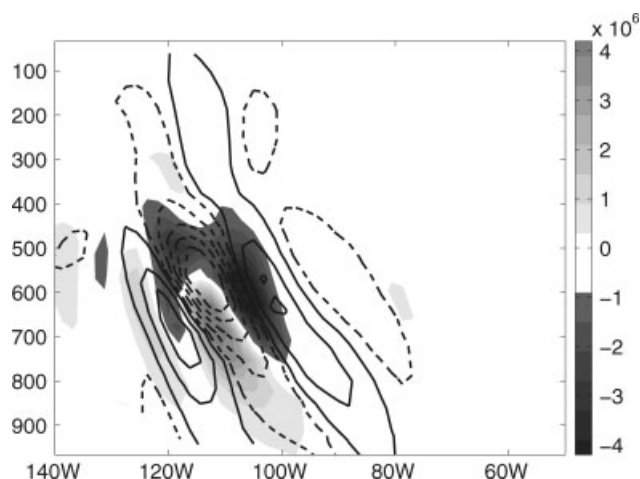


Figure 15. Adjoint sensitivity to moisture ($\partial J/\partial Q_0$) at $t = 0$ hours (grey shading) at 59°N. Black contours are the NLSV temperature perturbations as in Figure 10(a).

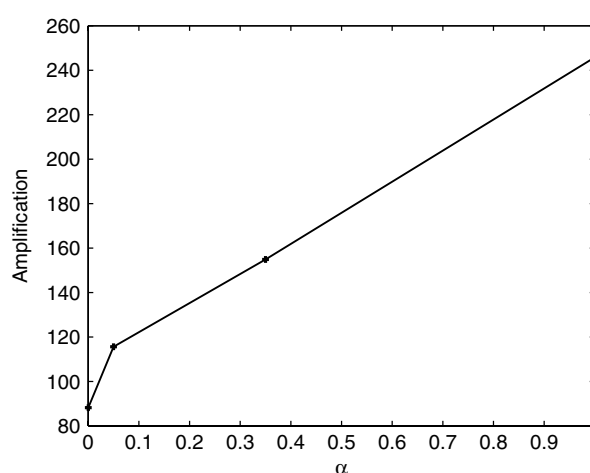


Figure 16. Amplification rate σ^2 as a function of α for the experiment where the constraint on water vapour is varied following (19).

The technique we have introduced here has the advantage that we can control the constraint on the water vapour field. To see how the growth rate is dependent on the amplitude of the perturbation, we replace the constraint on water vapour in (5) by

$$Q_0 + \Delta Q_0 \leq \inf\{Q_{\text{sat}}(T_0), \alpha \max_{\text{level}}(Q_0 + \Delta Q_0)\}, \tag{19}$$

where α is a parameter varying between 0 and 1. Figure 16 shows a rapid increase of amplification for small α that becomes linear when α becomes larger. This curve is of particular interest since it represents the sensitivity of predictability with respect to the variation of moisture of the basic state. It should be noted that, even for a modest value of α (around 0.2), there is an increase of around 50% of amplification, illustrating the important role played by moisture in predictability.

5. Conclusion

We have presented a nonlinear method for measuring sensitivity to moisture, extending the concept of sensitivity to a fully nonlinear framework. We stress that we do not impose the linear assumption which may not be valid in presence of moist physics. Using constrained nonlinear optimization, we obtained the modification of the basic state moisture field associated with the largest nonlinear growth of perturbations (NLSVs). The results demonstrate that a localized modification of the initial moisture field allowed optimal growth of NLSV, larger than if the whole atmosphere were saturated at initial time. The growth rate of NLSV over 24 hours is then increased by a factor of almost 3 in comparison with the reference case. That enhancement of the amplification is mainly due to diabatic effects, the modification of the moisture field increasing only slightly the baroclinicity of the trajectory. However in the two cases the shape and structure of the optimal perturbations remain quite similar. This indicates that, for the particular case we examined, the mechanism

of perturbation growth remains basically unchanged and that the role of diabatic effects is to reinforce the dry baroclinic instability mechanism. This is possible because diabatic tendencies due to precipitation and temperature perturbations are in phase, allowing the largest growth without modifying the structure of the perturbations. The optimal moisture modification, located at initial time in the lower troposphere (mainly below 700 hPa), is then advected eastwards in the middle troposphere within the warm conveyor belt of a developing cyclone.

Even if we only examined one case, we think that the basic processes we have unveiled should be at play in other situations as well. In the present simulation, we did not find a moist perturbation in a different location from the dry one. However we believe that there may be instances where moist processes will be sufficient to trigger a very strong growth rate, without the help of baroclinic processes (as in the diabatic Rossby wave scenario). Indeed other studies (Coutinho *et al.*, 2004; Hoskins and Coutinho, 2005) have identified moist singular vectors in other locations than their dry counterparts. This was also found in our model in a preliminary work (Rivière, 2007).

If this nonlinear moist sensitivity technique is a relevant tool for the study of sensitivity to moisture, it can also be applied to the study of other processes where the linear assumption may not hold.

Acknowledgements

G. L. is supported by an ANR grant (ENVISTORM, JCJC06-139163).

Appendix

Derivation of the gradient of the cost function (3)

The numerical nonlinear optimization code needs the gradient of the cost function,

$$J(\Delta\mathbf{X}_0, \delta\mathbf{x}_0) = \frac{E(\delta\mathbf{x}(t = \tau))}{E(\delta\mathbf{x}_0)} \quad (\text{A.1})$$

with respect to both variables $(\Delta\mathbf{X}_0, \delta\mathbf{x}_0)$. We recall that the perturbation at time t reads

$$\delta\mathbf{x}(t) = \mathbf{M}(\mathbf{X}_0 + \Delta\mathbf{X}_0 + \delta\mathbf{x}_0) - \mathbf{M}(\mathbf{X}_0 + \Delta\mathbf{X}_0). \quad (\text{A.2})$$

Taking the gradient of (A.1) in $\delta\mathbf{x}_0$ gives

$$\frac{\partial J}{\partial(\delta\mathbf{x}_0)} = \frac{1}{E(\delta\mathbf{x}_0)} \frac{\partial E(\delta\mathbf{x}(t = \tau))}{\partial(\delta\mathbf{x}_0)} - \frac{E(\delta\mathbf{x}(t = \tau))}{E(\delta\mathbf{x}_0)^2} \frac{\partial E(\delta\mathbf{x}_0)}{\partial(\delta\mathbf{x}_0)}. \quad (\text{A.3})$$

Writing the norm $E(\mathbf{Y}) = \langle \mathbf{Y}, \mathbf{Y} \rangle = \mathbf{Y}^T \mathbf{A} \mathbf{Y}$ where \mathbf{A} is the matrix of the scalar product associated with the norm

defined by (4),

$$\begin{aligned} E(\delta\mathbf{x}(t = \tau)) = & \langle \mathbf{M}(\mathbf{X}_0 + \Delta\mathbf{X}_0 + \delta\mathbf{x}_0), \mathbf{M}(\mathbf{X}_0 + \Delta\mathbf{X}_0 + \delta\mathbf{x}_0) \rangle \\ & + \langle \mathbf{M}(\mathbf{X}_0 + \Delta\mathbf{X}_0), \mathbf{M}(\mathbf{X}_0 + \Delta\mathbf{X}_0) \rangle \\ & - 2 \langle \mathbf{M}(\mathbf{X}_0 + \Delta\mathbf{X}_0 + \delta\mathbf{x}_0), \mathbf{M}(\mathbf{X}_0 + \Delta\mathbf{X}_0) \rangle. \end{aligned} \quad (\text{A.4})$$

Differentiating with respect to $\delta\mathbf{x}_0$ and using the adjoint $\mathbf{M}_{|\mathbf{X}_0 + \Delta\mathbf{X}_0 + \delta\mathbf{x}_0}^*$ about the trajectory $\mathbf{M}(\mathbf{X}_0 + \Delta\mathbf{X}_0 + \delta\mathbf{x}_0)$, we obtain

$$\begin{aligned} \frac{\partial E((\delta\mathbf{x})(t = \tau))}{\partial(\delta\mathbf{x}_0)} & = 2\mathbf{M}_{|\mathbf{X}_0 + \Delta\mathbf{X}_0 + \delta\mathbf{x}_0}^* \mathbf{A} \mathbf{M}(\mathbf{X}_0 + \Delta\mathbf{X}_0 + \delta\mathbf{x}_0) \\ & \quad - 2\mathbf{M}_{|\mathbf{X}_0 + \Delta\mathbf{X}_0 + \delta\mathbf{x}_0}^* \mathbf{A} \mathbf{M}(\mathbf{X}_0 + \Delta\mathbf{X}_0) \\ & = 2\mathbf{M}_{|\mathbf{X}_0 + \Delta\mathbf{X}_0 + \delta\mathbf{x}_0}^* \mathbf{A} \delta\mathbf{x}(t = \tau). \end{aligned} \quad (\text{A.5})$$

In this expression, $\mathbf{M}_{|\mathbf{X}}^*$ is the projection on the dry variables of the adjoint model about the trajectory corresponding to the initial basic state \mathbf{X} (this is not the full adjoint because the initial perturbation $\delta\mathbf{x}_0$ is dry). Noting $E_0 = E(\delta\mathbf{x}_0)$ and $E_f = E(\delta\mathbf{x}(t = \tau))$, we obtain

$$\frac{\partial J}{\partial(\delta\mathbf{x}_0)} = \frac{2}{E_0} \mathbf{M}_{|\mathbf{X}_0 + \Delta\mathbf{X}_0 + \delta\mathbf{x}_0}^* \mathbf{A} \delta\mathbf{x}(t = \tau) - \frac{2E_f}{E_0^2} \mathbf{A} \delta\mathbf{x}_0. \quad (\text{A.6})$$

To obtain the gradient with respect to $\Delta\mathbf{X}_0$, we follow the same procedure. Taking the gradient of (A.1) in $\Delta\mathbf{X}_0$ gives

$$\frac{\partial J}{\partial(\Delta\mathbf{X}_0)} = \frac{1}{E(\delta\mathbf{x}_0)} \frac{\partial E(\delta\mathbf{x}(t = \tau))}{\partial(\Delta\mathbf{X}_0)}, \quad (\text{A.7})$$

since $E(\delta\mathbf{x}_0)$ depends only on $\delta\mathbf{x}_0$ and not on $\Delta\mathbf{X}_0$. Differentiating (A.4) with respect to $\Delta\mathbf{X}_0$ gives

$$\begin{aligned} \frac{\partial E(\delta\mathbf{x}(t = \tau))}{\partial(\Delta\mathbf{X}_0)} = & 2\mathbf{N}_{|\mathbf{X}_0 + \Delta\mathbf{X}_0 + \delta\mathbf{x}_0}^* \mathbf{A} \mathbf{M}(\mathbf{X}_0 + \Delta\mathbf{X}_0 + \delta\mathbf{x}_0) \\ & + 2\mathbf{N}_{|\mathbf{X}_0 + \Delta\mathbf{X}_0}^* \mathbf{A} \mathbf{M}(\mathbf{X}_0 + \Delta\mathbf{X}_0) \\ & - 2\mathbf{N}_{|\mathbf{X}_0 + \Delta\mathbf{X}_0 + \delta\mathbf{x}_0}^* \mathbf{A} \mathbf{M}(\mathbf{X}_0 + \Delta\mathbf{X}_0) \\ & - 2\mathbf{N}_{|\mathbf{X}_0 + \Delta\mathbf{X}_0}^* \mathbf{A} \mathbf{M}(\mathbf{X}_0 + \Delta\mathbf{X}_0 + \delta\mathbf{x}_0), \end{aligned} \quad (\text{A.8})$$

where $\mathbf{N}_{|\mathbf{X}}^*$ is the projection of the adjoint on the moisture variable only (because $\Delta\mathbf{X}_0$ is a perturbation in the water vapour field only). Rearranging this expression and using (2),

$$\begin{aligned} \frac{\partial E(\delta\mathbf{x}(t = \tau))}{\partial(\Delta\mathbf{X}_0)} = & 2\mathbf{N}_{|\mathbf{X}_0 + \Delta\mathbf{X}_0 + \delta\mathbf{x}_0}^* \mathbf{A} \delta\mathbf{x}(t = \tau) \\ & - 2\mathbf{N}_{|\mathbf{X}_0 + \Delta\mathbf{X}_0}^* \mathbf{A} \delta\mathbf{x}(t = \tau). \end{aligned} \quad (\text{A.9})$$

This gives the final result

$$\begin{aligned} \frac{\partial J}{\partial(\Delta\mathbf{X}_0)} = & \frac{2}{E_0} \mathbf{N}_{|\mathbf{X}_0 + \Delta\mathbf{X}_0 + \delta\mathbf{x}_0}^* \mathbf{A} \delta\mathbf{x}(t = \tau) \\ & - \frac{2}{E_0} \mathbf{N}_{|\mathbf{X}_0 + \Delta\mathbf{X}_0}^* \mathbf{A} \delta\mathbf{x}(t = \tau). \end{aligned} \quad (\text{A.10})$$

References

- Barkmeijer J. 1996. Constructing fast-growing perturbations for the nonlinear regime. *J. Atmos. Sci.* **53**: 3838–3851.
- Beare RJ, Thorpe AJ, White AA. 2003. The predictability of extratropical cyclones: Nonlinear sensitivity to localized potential vorticity perturbations. *Q. J. R. Meteorol. Soc.* **129**: 219–237.
- Buizza R. 1994. Sensitivity of optimal unstable structures. *Q. J. R. Meteorol. Soc.* **120**: 429–451.
- Coutinho MM, Hoskins BJ, Buizza R. 2004. The influence of physical processes on extratropical singular vectors. *J. Atmos. Sci.* **61**: 195–209.
- Duan WS, Mu M. 2006. Investigating decadal variability of ENSO asymmetry by conditional nonlinear optimal perturbation. *J. Geophys. Res.* **111**: C07015. doi: 10.1029/2005JC003458
- Duan WS, Mu M, Wang B. 2004. Conditional nonlinear optimal perturbations as the optimal precursors for ENSO events. *J. Geophys. Res.* **109**: D23105. doi: 10.1029/2004JD004756
- Ehrendorfer M, Errico RM, Raeder KD. 1999. Singular-vector perturbation growth in a primitive equation model with moist physics. *J. Atmos. Sci.* **56**: 1627–1648.
- Emanuel KA, Fantini M, Thorpe AJ. 1987. Baroclinic instability in an environment of small stability to slantwise moist convection. Part I: Two-dimensional models. *J. Atmos. Sci.* **44**: 1559–1573.
- Errico RM. 1997. What is an adjoint model? *Bull. Amer. Meteorol. Soc.* **78**: 2577–2591.
- Farrel BF. 1989. Optimal excitation of baroclinic waves. *J. Atmos. Sci.* **46**: 1193–1206.
- Fraedrich K, Jansen H, Kirk E, Luksch U, Lunkeit F. 2005. The planet simulator: Towards a user friendly model. *Meteorol. Zeitschrift* **14**: 299–304.
- Gilmour I, Smith LA, Buizza R. 2001. Linear regime duration: Is 24 hours a long time in synoptic weather forecasting? *J. Atmos. Sci.* **58**: 3525–3539.
- Gutowksi WJ, Branscome LE, Stewart DA. 1992. Life cycles of moist baroclinic eddies. *J. Atmos. Sci.* **49**: 306–319.
- Hohenegger C, Schär C. 2007. Atmospheric predictability at synoptic versus cloud-resolving scales. *Bull. Amer. Meteorol. Soc.* **88**: 1783–1793.
- Hoskins BJ, Coutinho MM. 2005. Moist singular vectors and the predictability of some high-impact European cyclones. *Q. J. R. Meteorol. Soc.* **131**: 581–601.
- Lacarra J-F, Talagrand O. 1988. Short-range evolution of small perturbations in a barotropic model. *Tellus* **40A**: 81–95.
- Langland RH, Elsberry RL, Errico RM. 1996. Adjoint sensitivity of an idealized extratropical cyclone with moist physical processes. *Q. J. R. Meteorol. Soc.* **122**: 1891–1920.
- Lapeyre G, Held IM. 2004. The role of moisture in the dynamics and energetics of turbulent baroclinic eddies. *J. Atmos. Sci.* **61**: 1693–1710.
- Le Dimet F-X, Ngodock H-E, Luong B. 1997. Sensitivity analysis in variational data assimilation. *J. Meteorol. Soc. Japan* **75**: 145–155.
- Mahfouf J-F, Buizza R. 1996. 'On the inclusion of physical processes in linear forward and adjoint models impact of large-scale condensation on singular vectors'. *ECMWF Newsletter* **72**: 2–8.
- Moore RW, Montgomery MT. 2004. Reexamining the dynamics of short-scale, diabatic Rossby waves and their role in midlatitude moist cyclogenesis. *J. Atmos. Sci.* **61**: 754–768.
- Moore RW, Montgomery MT. 2005. Analysis of an idealized, three-dimensional diabatic Rossby vortex: A coherent structure of the moist baroclinic atmosphere. *J. Atmos. Sci.* **62**: 2703–2725.
- Mu M. 2000. Nonlinear singular vectors and nonlinear singular values. *Sci. China (D)* **43**: 375–383.
- Mu M, Duan WS, Wang B. 2003. Conditional nonlinear optimal perturbation and its applications. *Nonlin. Proc. Geophys.* **10**: 493–501.
- Mu M, Zhang Z. 2006. Conditional nonlinear optimal perturbations of a two-dimensional quasigeostrophic model. *J. Atmos. Sci.* **63**: 1587–1604.
- Parker DJ, Thorpe AJ. 1995. Conditional convection heating in a baroclinic atmosphere: A model of convective frontogenesis. *J. Atmos. Sci.* **52**: 1699–1711.
- Pavan V, Hall N, Valdes P, Blackburn M. 1999. The importance of moisture distributions for the growth and energetics of midlatitude systems. *Ann. Geophysicae* **17**: 242–256.
- Rabier F, Courtier P, Talagrand O. 1992. An application of adjoint models to sensitivity analysis. *Beitr. Phys. Atmos.* **65**: 177–192.
- Rabier F, Klinker E, Courtier P, Hollingsworth A. 1996. Sensitivity of forecast errors to initial conditions. *Q. J. R. Meteorol. Soc.* **122**: 121–150.
- Rivière O. 2007. 'Prévisibilité de l'écoulement atmosphérique aux échelles synoptiques: influence des non-linéarités et de l'humidité'. Doctoral thesis. L'Ecole Nationale des Ponts et Chaussées: Marne-la-Vallée, France.
- Rivière O, Lapeyre G, Talagrand O. 2008. Nonlinear generalization of singular vectors in baroclinic unstable flows. *J. Atmos. Sci.* **65**: 1896–1911.
- Snyder C, Joly A. 1998. Development of perturbations within growing baroclinic waves. *Q. J. R. Meteorol. Soc.* **124**: 1961–1983.
- Spyksma K, Bartello P. 2007. Predictability in wet and dry convective turbulence. *J. Atmos. Sci.* **65**: 220–234.
- Talagrand O. 1991. 'Adjoint models'. Pp 73–91 in *Proceedings of seminar on numerical methods in atmospheric models. September 1991. II*. ECMWF: Reading, UK.
- Tan Z, Zhang F, Rotunno R, Snyder C. 2004. Mesoscale predictability of moist baroclinic waves: Experiments with parametrized convection. *J. Atmos. Sci.* **61**: 1794–1804.
- Wächter A, Biegler LT. 2006. On the implementation of a primal-dual interior point filter line search algorithm for large-scale nonlinear programming. *Math. Program.* **106**: 25–57.
- Wernli H, Dirren S, Liniger MA, Zillig M. 2002. Dynamical aspects of the life cycle of the winter storm 'Lothar' (24–26 December 1999). *Q. J. R. Meteorol. Soc.* **128**: 405–429.
- Zhang F, Bei N, Rotunno R, Snyder C, Epifanio CC. 2007. Mesoscale predictability of moist baroclinic waves: Convection-permitting experiments and multistage error growth dynamics. *J. Atmos. Sci.* **64**: 3579–3594.
- Zou X. 1993. Variational data assimilation with moist threshold processes using the NMC spectral model. *Tellus* **45A**: 370–387.